Department of Physics and Astronomy

University of Heidelberg

Master thesis

in Physics

submitted by

Alexander Karl Sivitilli

born in Renton

2016

Design and Implementation of a Laser Alignment Telescope for ARGOS on the Large Binocular Telescope

This Master thesis has been carried out by Alexander Karl Sivitilli

at the

Max-Planck-Institute for Astronomy

under the supervision of

Prof. Dr. Klaus Meisenheimer

Acknowledgments

In the darkest of times with one's labors, it is the help of others that can be the promising beacons that restore hope in one's own ability. The LAT project was no exception to this phenomenon. The success of my work would not have been as readily attainable were it not for the help of the following people. Their contributions to the project were not only critical to its success, but also necessary for its enjoyment. With that, I hereby acknowledge...

Wolfgang Gässler for his support and guidance as my mentor. He was always an email or knock at the door away from leading me out of the most tangled of issues.

Klaus Meisenheimer for supervising the thesis and providing feedback on the project direction.

Martin Kürster for acting as second examiner despite my request taking him by surprise.

Jose Luis Borelli for helping me sort out my software bugs, comprehend the mysteries of software development, and make the LAT great again.

Martin Kulas for helping integrate the SLA into the ARGOS architecture and answering my absurd questions.

The Italians, Lorenzo Busoni and Marco Bonaglia for their patience with the LAT integration and always keeping the spirits of the team high.

Sebastian Rabien for his leadership of ARGOS and keeping expectations high.

Gustavo Rahmer and the rest of the LBTO staff for keeping us safe and for offering a pleasant stay at their fine Large Binocular Telescope.

Julian Ziegleder, Gilles Orban de Xivry and Diethard Peter for offering their expertise and knowledge wherever it was needed.

Haus der Astronomie for allowing me access to a Celestron mount for LAT testing.

My mother Ursula, who has always given her love and emotional support, no matter from how far away.

My father Victor, who has always encouraged me to achieve what lay on the horizon.

My younger brother Dominic, who is always keen on discussing our latest findings of the universe.

My older brother Tony, who has always kept me aware of the beauty behind mechanics.

Carmia Schoeman for her amazing ability to keep me in a state of calm, no matter how stressed, tired or overworked I find myself. And for sharing with me her love of science and intellectual discourse. And for always remaining pretty cool.

Zusammenfassung

Adaptive Optik (AO) Systeme werden bei bodengebunden astronomischen Teleskopen weltweit zunehmend implementiert. Unter Zuhilfenahme von natürlichen oder künstlichen Leitsternen, kann die Störung des Lichts, das sich durch turbulente Atmosphäre ausbreitet, als eine Wellenfront quantifiziert und abgebildet werden. Diese Wellenfront wird dann von einem vorformbaren Spiegel korrigiert. Dadurch entsteht eine höhere Auflösung in den wissenschaftlichen Bilder der astronomischen Objekten.

Das Advanced Rayleigh guided Ground layer adaptive Optics System (ARGOS) wird gerade beim Large Binocular Teleskop (LBT) in Betrieb genommen. Dieses einzigartige AO-System vermindert Wellenfrontfehler in einem 4' x 4' Feld mit Hilfe seiner sechs künstlichen Leitsternen. Wegen der Krümmung und Instandhaltung des LBTs, können die Laser falsch ausgerichtet werden. Daher müssen sie häufig manuell korigiert werden. Um Zeit und Arbeitskraft zu sparen, ist eine automatische Ausrichtung der Laser notwendig.

Diese Masterarbeit beschreibt sowohl den Aufbau und die Implementierung des Laser Alignment Teleskops (LAT), der von den Laser Bilder macht, als auch des Smart Laser Alignment (SLA) Algorithmus, der automatisch die Laser identifiziert und sich auf ihre Wellenfront-Sensoren ausrichtet.

Abstract

Adaptive optics (AO) systems are increasingly being implemented at earth-bound astronomical telescopes around the world. With the aid of natural or artificial guide stars, the distortion of light moving through the turbulent atmosphere can be mapped as a wavefront that is then corrected with a deformable mirror. The result is higher resolutions for scientific images of celestial objects.

One such system is the Advanced Rayleigh guided Ground layer adaptive Optics System (ARGOS) currently being commissioned at the Large Binocular Telescope (LBT). This AO set-up is unique in that it harnesses six artificial laser guide stars to correct wavefronts over a wide 4' x 4' field. Due to telescope flexure and maintenance, lasers can become misaligned from the wavefront sensors of ARGOS, requiring frequent manual realignment. In order to save time in both commissioning and operation of ARGOS, an automatic alignment of the lasers with the wavefront sensors is needed.

This thesis describes the construction and implementation of a Laser Alignment Telescope (LAT) for acquiring images of the launched lasers. In addition, an accompanying Smart Laser Alignment (SLA) algorithm will be written to automatically identify and align the lasers to their respective wavefront sensors.

Contents

Part I

Background

1 Introduction

In recent decades, it has become increasingly common for ground-based telescopes worldwide to implement Adaptive Optics (AO) systems to overcome wavefront distortions caused by atmospheric turbulence (see figure 1.1). When light from a celestial object enters Earth's atmosphere, the various local perturbations of pressure and temperature caused by the moving air leads to a variation of the optical refractive indices along the medium of the incident wavefronts. What results is "atmospheric seeing," or a distortion of the wavefronts from parallel sheets to mangled membranes, effectively blurring the images taken of the celestial objects.

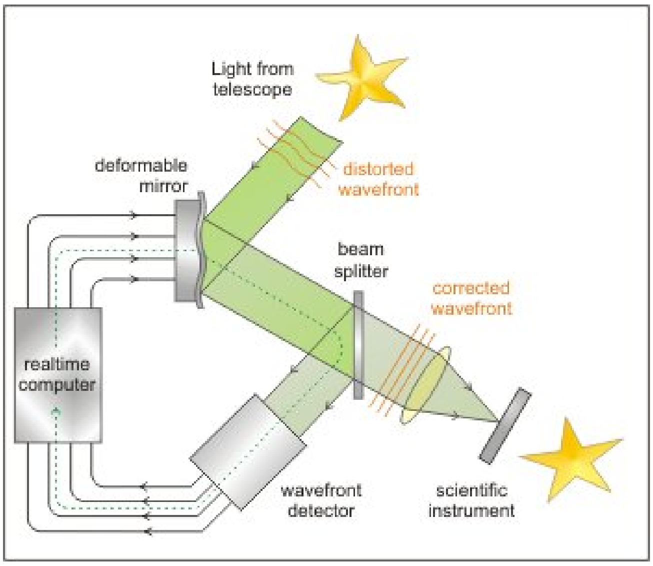

Figure 1.1: Scheme of an AO system in action. Light from a guide star enters and is split into the wavefront detector. The distortions are mapped and a deformable mirror is deformed to compensate for them, correcting all incoming wavefronts as a result. Image courtesy of Ziegleder [2009]

By use of a reference point source of light above the layers of turbulence, an AO system installed on a ground-based telescope can quantify these distortions on the wavefront. The system then uses a deformable mirror installed for the individual instruments or, as in the case of the Large Binocular Telescope, integrated into the telescope's main optics, to compensate for the distortions in real-time (Esposito et al. [2011]). Observing instruments can then benefit with higher resolutions and better point spread functions of scientific targets. Early AO systems used natural guide stars (NGS) as a point source of light, which limited the targets that can benefit to ones with bright stars in the field of view (FOV). The newer and more preferred light point source is an artificial laser guide star (LGS) that focuses to a point above the turbulent-rich layers of the atmosphere and opens up broadly the list of targets that can benefit from AO wavefront corrections. There are currently two popular flavors of LGSs, Sodium guide stars and Rayleigh guide stars. The former relies on a particular wavelength (589.2 nm) of laser light to stimulate a spot of fluorescence in the sodium layer at an altitude of about 95km. The latter propagates a laser tuned at wavelengths to stimulate high amounts of Rayleigh scattering at lower altitudes, from which the laser extinguishes around 20km. In order to extract an artificial LGS from this system, the beam is sent out in pulses and a wavefront sensor (WFS) uses the delay in a high speed shutter relying on the Pockels effect to image the pulse when it reaches a particular altitude (Rabien et al. [2008]).

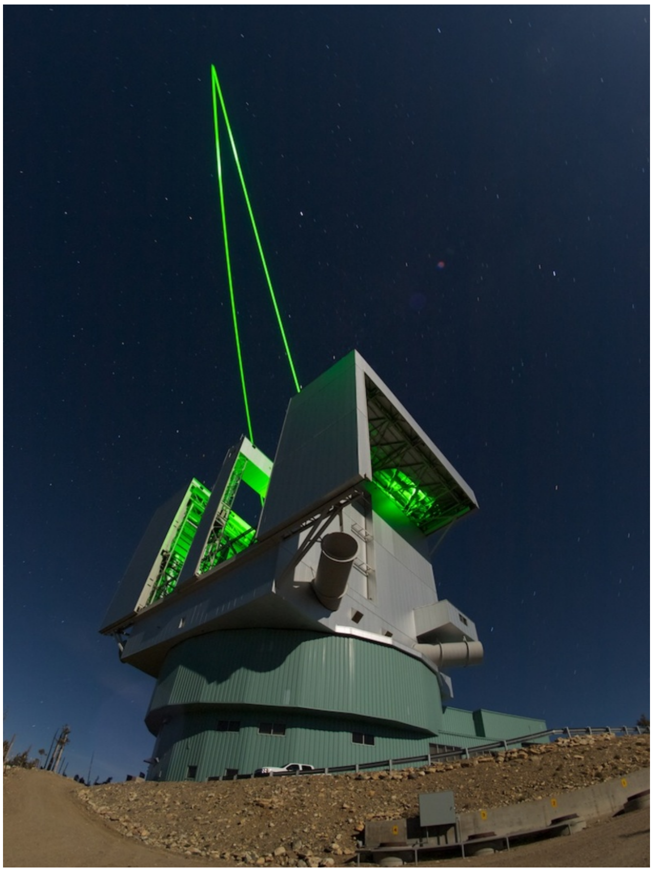

Figure 1.2: LBT with ARGOS Rayleigh lasers propagating into the sky. Note that slices of these beams are "gated" onto the WFSs to produce the LGSs. Image courtesy of ARGOS [2014]

The Advanced Rayleigh guided Ground layer adaptive Optics System (ARGOS) is an AO system currently undergoing commissioning at the Large Binocular Telescope on Mt. Graham in Arizona. ARGOS takes the Rayleigh LGS system a step further by harnessing the power of three LGSs per mirror on the telescope for a total constellation of six lasers beaming into the heavens. The use of multiple LGSs will allow observers at the LBT to harness the benefits of AO over a widefield of 4' x 4', making it ideal for the new wide field imager and multi-object spectrograph, LUCI I and II, also currently in its commissioning phase at the LBT. Scientific benefits expected by ARGOS include increased point source sensitivity, increased slit coupling efficiency with spectroscopy, and overall enhanced spatial resolution (Rabien et al. [2008]).

One complication that has already cost the ARGOS team a cumulation of many hours of commissioning time, and could impact observing time for future astronomers hoping to benefit from the AO system, is the alignment of the lasers with the ARGOS WFSs. Manual alignment by a "fishing" method has already proven time consuming and with the unpredictable weather conditions on Mt. Graham, this time is very precious, so a solution was sought. In order to save time with both the commissioning and operation of the ARGOS system, a Laser Alignment Telescope (LAT) was constructed and installed along with a complimentary Smart Laser Alignment (SLA) algorithm to automatically align the ARGOS LGSs with their respective WFSs. Not only will the LAT be an essential component in saving hours of observing time previously dedicated to manual alignment of the lasers, but the LAT also replaces the aging multi-use Mount Alignment Telescope (MAT), an instrument previously installed with both narrow-field (MAT-NF) and wide-field (MAT-WF) components to aid in problems with telescope pointing or to monitor clouds crossing the LBT target field (Hill [2015]). The LAT can be considered an upgrade of the MAT with newer components and higher-resolution over a wider field in addition to having better protection from the elements with its own housing. The LAT therefore will also be made available to other users by handing over the server software directly to the LBT staff upon completion.

The following master thesis will review the design process, in addition to the construction and implementation, of both the LAT and SLA for ARGOS. The next chapter will continue the project background by touching on the concept behind the ARGOS system and why we need the lasers aligned. The next part will first describe the hardware and software giving life to the LAT. This will then be followed up with the details on the building, testing, installation and alignment of the telescope, a process which required several on-site commissioning trips to the LBT. The next part will then introduce the LAT's accompanying SLA algorithm and the development undergone to produce the final product. First, the various computer vision strategies attempted to detect and distinguish lasers will be mentioned in addition to their benefits and drawbacks. The method of locating the actual LGS in the discovered beams will then be described. Finally, the process of integrating the SLA with the ARGOS architecture and how movement corrections to the lasers are actually applied will be mentioned. The last part will explore project results and possible future improvements in addition to concluding the thesis.

2 ARGOS

In order to correct wavefronts distorted by the atmosphere, each LGS launched by ARGOS needs to be imaged by its respective WFS. This is done by pulsing the lasers and delaying the Pockels cell shutters on each WFS so that they open $2 * 12km/c \approx 80.06\mu s$ after the launch of the pulse (Rabien et al. [2010]). This allows only a slice of light at 12km to enter the sensor, but the lasers must have their 12km points aligned with the WFSs for them to enter at all.

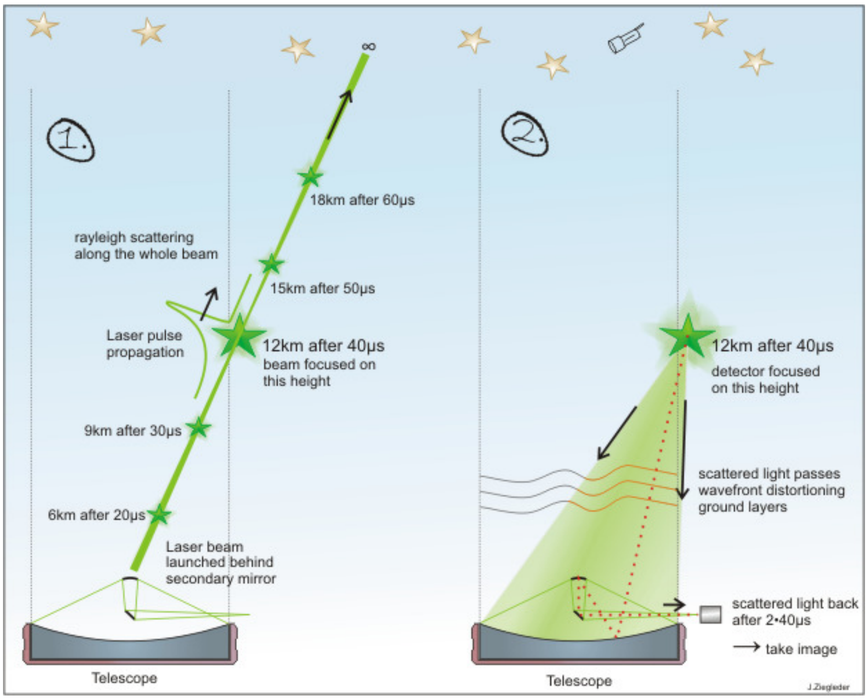

Figure 2.1: A graphical representation of AROGS pulsing a laser to 12km and imaging the resultant Laser Guide Star that has passed through the turbulent atmosphere. Photo courtesy of Ziegleder [2009]

For each LBT side, the returning laser light is split off from the main optical path of the LBT with a dichroic beam splitter and enters the WFS (see figure 2.2). The entrance to the WFS consists of three small holes surrounded by mirror from which the light can be reflected into the system's "patrol cameras". When the laser is not aligned with the holes, this set-up allows fine adjustment of the angle of the launched lasers so they can be steered into the entrance. These patrol cameras each possess a FOV of 1', so in order for the laser to be imaged, the 12km points on the lasers must be aligned to within 30" of the centers of these cameras. Note that on each LBT side, the main launch mirror of the lasers (LM1) moves the laser triplet as a group, so to simplify things, the potential alignment system will control these specific mirrors to steer each laser triplet rather than controlling and aligning individual lasers.

Once the lasers are imaged anywhere on the patrol cameras (see figure 2.3), the automated ARGOS LGS Acquisition system can finely align the lasers to the centers, allowing the LGSs to enter the WFS holes. Prior to the LAT project, manual adjustment of the lasers was necessary to move the LGSs from a wider offset to within the 30" necessary for this system. We wanted our new instrument and algorithm to automate this process.

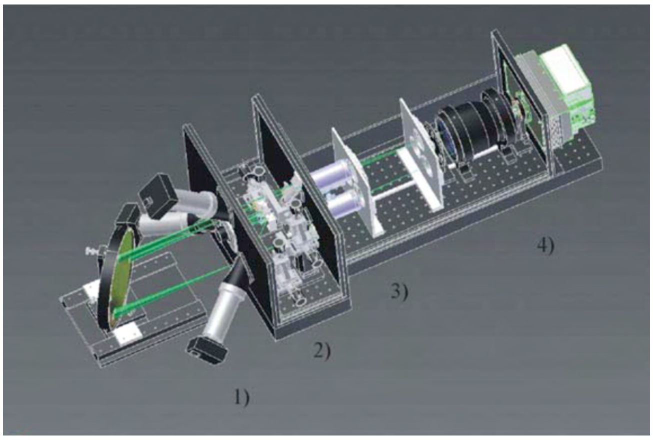

Figure 2.2: Model of one of the two WFS units with the three patrol cameras in position (1) sticking out the left side to image reflected laser light. Image courtesy of Rabien et al. [2010]

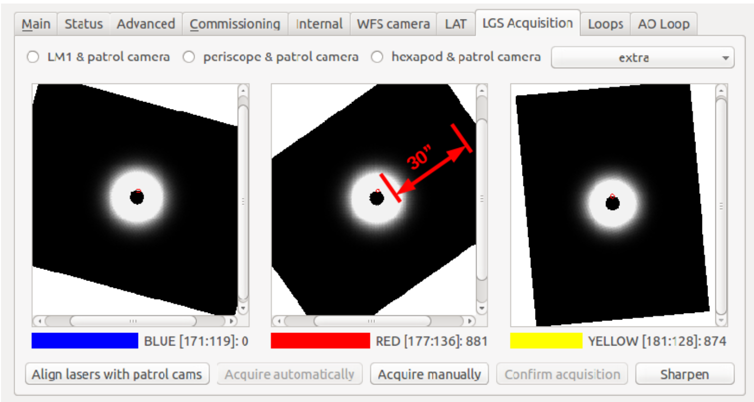

Figure 2.3: Screen shot taken of ARGOS LGS Acquisition system with patrol camera images spanning 1' each with simulated LGSs correctly aligned with the WFS holes

3 Project Expectations

The following sections itemize the tasks we set out to accomplish with the two main parts of the masters project.

3.1 Laser Alignment Telescope

- Construct the Laser Alignment Telescope (LAT) to replace the aging Mount Alignment Telescope (MAT)
- Choose LAT components that combine the FOV of the MAT-WF (1.43 x 0.95 degrees) with the pixel scale of the MAT-NF (1.62"/pixel)
- Assemble a housing for the the LAT in a case that protects it from the elements
- Combine the available drivers and commands for the components into a single LATServer program as the control software
- Package the control software in a form that can be integrated into and run from the LBT architecture and accessed by multiple general users (outside of ARGOS)

3.2 Smart Laser Alignment Algorithm

- Write a script that takes an image of the ARGOS lasers and aligns their 12km points along each laser to within 30" of their respective patrol camera centers
- Design the script to require as little user interaction as possible upon execution
- Integrate the script into the ARGOS architecture with possible control from both the Linux command line (CL) and a graphical user interface (GUI) to be built by the ARGOS engineers
- Build into the code a preliminary height analysis script that uses laser geometry and a Rayleigh light scattering model to allow future expansion to improve alignment in cloudy conditions

Part II

Laser Alignment Telescope

4 Laser Alignment Telescope

The first part of the project was the design, prototyping, construction, and installation of the LAT hardware and its control software. This required several trips to both the MPE in Garching and the LBT in Arizona.

Chapter 5 details the main components of the LAT and why they were chosen. Chapter 6 covers the control software and server-client interface for using the LAT. Finally, Chapter 7 goes over the testing, assembly, mounting and alignment of the LAT for final installation on the LBT.

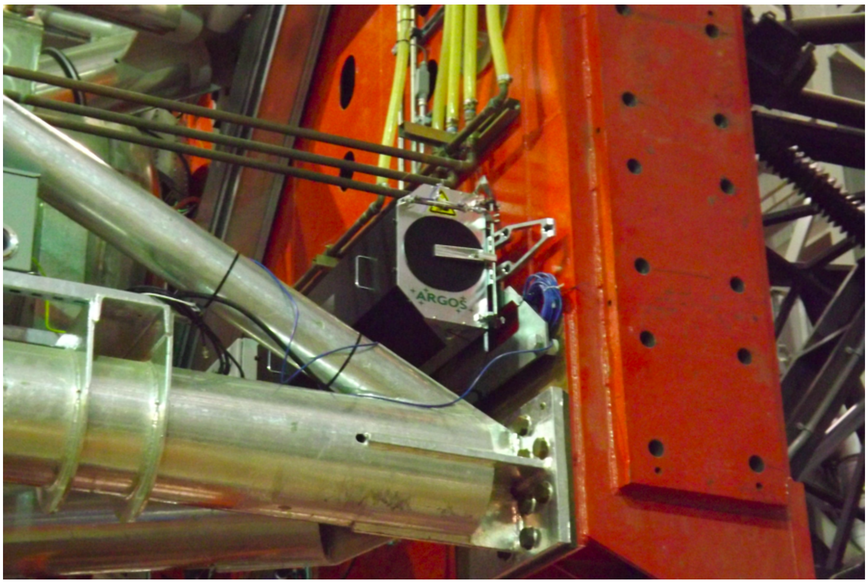

Figure 4.1: The LAT assembled and mounted in its final designated space on the front left (SX) C-ring extension of the LBT

5 Hardware Components

As mentioned in chapter 3, we wanted our hardware to have capability close to that of the MAT if not an improvement. The technical goals we set for the LAT components are the following:

FOV	1.43 x 0.95 degrees
Pixel scale	1.62"/pixel
Control	Linux drivers
Other	Protected

Table 5.1: Technical details we desired for the LAT

5.1 Camera

For the camera we chose the Allied Vision Technologies (AVT) Prosilica GE 2040. We required a relatively high resolution when imaging of the lasers; this would provide not only the detail needed for distinguishing lasers from each other and celestial objects when implementing the finding component of the Smart Laser Alignment (SLA) algorithm for which crisp laser peaks separate from background noise will be needed, but it would also enable the algorithm to find clean integrated flux profiles of each laser before proceeding with alignment. Such clean profiles could also be used for optional laser height analysis. If we take this camera's 2048 x 2048 pixel resolution and divide it into 1 degree, a FOV close to that of the MAT-WF which we set as our goal, we achieve a pixel scale of 1.76"/pixel. This is fairly close to the desired pixel scale comparable to the MAT-NF (1.62"/pixel), making this particular camera's resolution satisfactory for the LAT. Although higher resolution cameras are available, the increased cost and higher network load from larger image sizes make the improved pixel scale not worth the upgrade.

Because the primary purpose of the LAT is to save time with ARGOS laser alignment in addition to its replacement of the general use MAT, it is important that the camera and its acquisition software exhibit the ability to acquire and process images quickly. The binning ability of this camera satisfies this where adjacent pixels are summed according to the binning factor. This decreases readout time of the CCD at the cost of spatial resolution (Léna et al. [2012]).

Due to the constrained time frame of the project, it was also preferable to use a camera for which there already existed a degree of familiarity among colleagues in the MPIA Instrumentation department. AVT's cameras have been used in several projects within the MPIA instrumentation department including with ARGOS itself.

As there is no on/off capability for the camera, power would need to be directly cut from the camera in order to shut it down when not in use. This would be handled by the stepper motor controller by one of its digital outputs and a relay switch. Also note that the AVT camera requires a threaded standard C-mount to attach a lens.

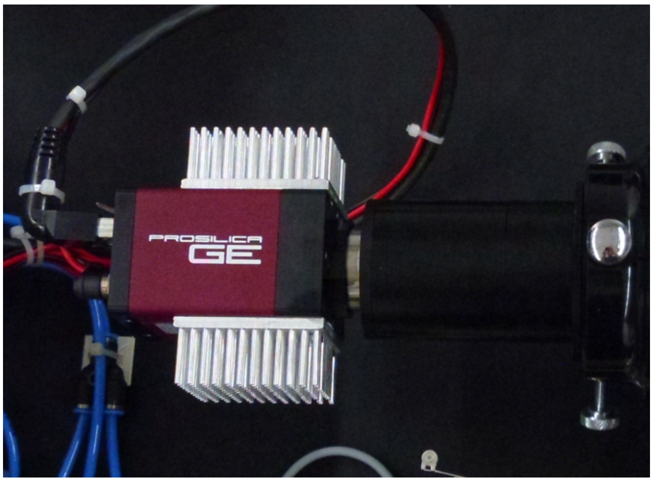

Figure 5.1: Camera attached to the LAT telescope via a C-mount adapter. Due to relatively high operating temperatures, two passive heat sinks were attached to the top and bottom upon final installation

Resolution	2048 x 2048 pixels
Pixel scale with 1° FOV	1.76"
Image depth	8,12 bits
Horizontal binning ability	1-8
Vertical binning ability	1-2048
Driver availability	Windows, Linux

Table 5.2: Notable technical specifications of the camera

5.2 Telescope

The LAT itself is a TS 152mm f/5.9 Refractor made by Teleskop Service. The MAT predecessor had two telescopes that provided its wide-field (MAT-WF) and narrow-field (MAT-NF) capabilities. Previous laser imaging with the MAT-WF suggested that a similar field of view of around 1 degree should suffice for alignment of both SX (left-side) and DX (right-side) lasers with the MAT-NF pixel scale of about 1.62"/pixel as a goal for the resolution. The AVT camera introduced in the previous section has a square sensor size of 15.2x15.2 mm which, when paired with the LAT's plate scale of 230"/mm, achieves a final FOV of about 58'x58' or 0.97 x 0.97 degrees, very close to the MAT-WF. In addition, we achieve a pixel scale on the LAT of 1.7", comparable to that of the MAT-NF. Thus we now effectively combine the wide-field of the MAT-WF with a small pixel scale close to that of the MAT-NF. The telescope is shown in figure 5.2.

A unique feature of the telescope is the Dual Speed Crayford (DSC) focuser, a mechanism commonly reserved for higher-level amateur telescope systems. The DSC works similar to a a rack and pinion adjustment system, but without teeth. A spring-loaded rod controlled by the focus knobs smoothly moves a flat plate embedded in the focus tube by friction, allowing the focus to be adjusted without wobble or backlash. This allows for a reasonable amount of precision for focus adjustment at low cost, however in chapter 15 we will see how this introduces potential problems that may require changes at a later date.

Figure 5.2: LAT undergoing testing at MPIA. The test mount, finderscope, and eyepiece pictured were later removed in the final set-up

type	refractor
f-number	f/5.9
diameter	152 mm
plate scale	230 "/mm

Table 5.3: Notable technical specifications of the LAT

5.3 Electronic Focus

The LAT needs an adjustable focus that can be controlled remotely. This is necessary to make sure the SLA receives sharp images of the laser beams throughout the night as change in temperature could potentially require fine readjustment of the focus. To accomplish this, the fine adjustment knob on the DSC focuser was replaced by a coupling to a two-phase QMOT QSH4218 hybrid stepper motor which is controlled by a Nanotec SMCI33-2 stepper motor control. This arrangement provides precision to around a calculated 9 micrometer focus adjustment per step of the motor. Consistent positioning of the focus for optimal laser imaging in addition to damage prevention calls for the inclusion of limit switches at both home and end positions of the LAT focus that can be triggered by an attached metal sleeve on the focuser tube of the LAT. Note that the motor controller requires an RS-485 serial port connection from the server computer to function, which can be difficult to connect on site at the LBT due to a lack of serial ports on the telescope itself. We therefore use a MOXA Nport 5150 serial device server (SDS) that allows serial communication over an Ethernet cable from the server.

In order to calculate the position precision of the electronic focus adjustment, a range of step positions were set after which calipers accurate to within 0.01 mm were used to measure the physical distance (the red line in figure 5.3) of the metal sleeve from the focus mechanism. The slope of the fitted line (see figure 5.4) then revealed the precision as 9 micrometers per step. Note that step position 0 is when the focus position is closest to the LAT and the maximum 9000 is when furthest, giving a focus adjustment range of 81 cm.

adjustment precision	9 μm / step
home step position (telescope end)	0 steps 0 cm
maximum step position (camera end)	9000 steps 8.1 cm

Table 5.4: Notable technical specifications of the electronic focus

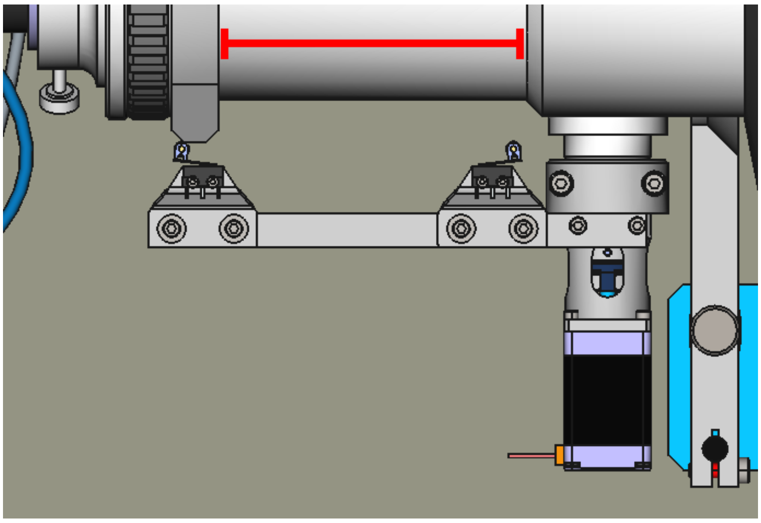

Figure 5.3: CAD model close-up of DSC knob replaced by coupling to stepper motor and focus end-switch rail with both home and end switches mounted. Note the distance marked in red is that measured for the precision calculation in figure 5.4.

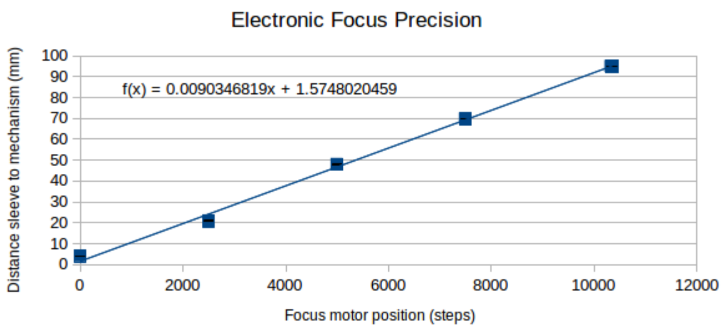

Figure 5.4: Plot of data and fitted line to calculate electronic focus precision. The slope of the line shows the precision in mm. Note the error bars for the focus distance are not visible do to their 0.01 mm length being very short on the plot.

5.4 Housing

It was important that the LAT and its components were mounted in a covered and protected configuration on the LBT. Exposure to the elements could cause a range of problems including obstructing particles on the lens or damaging dust on the LAT's sensitive DSC focuser (see chapter 15). The LAT also required the ability to be finely adjusted along elevation and altitude with minimal flexing deviations once the final alignment was found. The adjustment is accomplished by two manual differential adjustment screws in these respective directions against which the mount is spring loaded. Equipped with two indicators, these fine adjustments can be converted to angle measurements and ultimately pixel distances of the LAT images to align the LAT with the optical axis of the LBT telescope (see section 7.4). The housing design was outsourced to an engineer in Munich with the final material cutting and assembly taking place at the MPE in Garching.

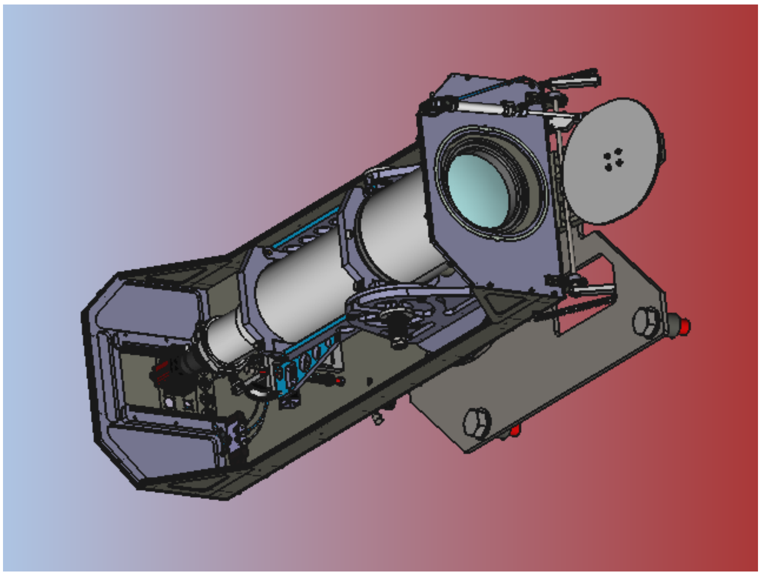

Figure 5.5: CAD model of the LAT housing with cover missing. Design was drafted by Christian Rehm in Isen.

Altitude precision Altitude adjustment	10 micron clockwise points telescope up
Azimuth precision Azimuth adjustment	10 micron clockwise points telescope right

Table 5.5: Notable technical specifications of Housing.

5.5 Dust-shutter

The housing also includes a dust-shutter that opens and closes using a compressed air hydraulic system driven by a Festo CPE14-M1BH-5L-1/8 valve. Similar to the camera power, control of the shutter valve happens via a relay connected to a digital output on the stepper motor controller. The shutter is opened when the output has power and closed when its off. A nice advantage of this is that if power is cut to the system, the shutter is automatically closed to protect the LAT.

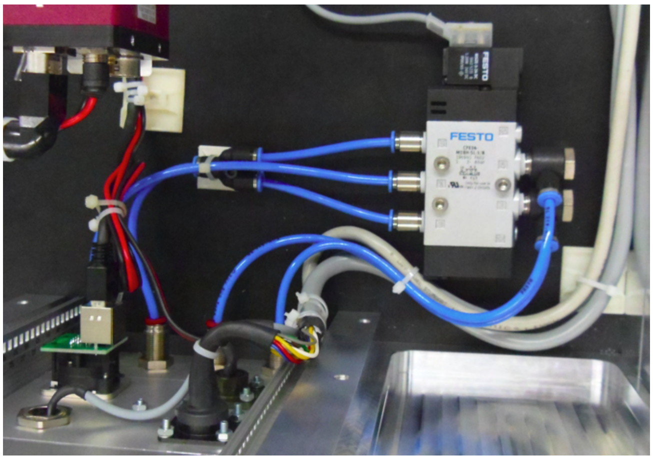

Figure 5.6: Festo valve with relay power connected at top

5.6 Requirements Recap

Specification	Minimum	LAT
FOV	1.43 x 0.95 degrees	0.97 x 0.97 degrees
Pixel scale	1.62"/pixel	1.7"/pixel
Drivers	Linux	Linux & Windows
Protected	no	yes

Table 5.6: Final check of components satisfaction of LAT requirements

6 Control Software

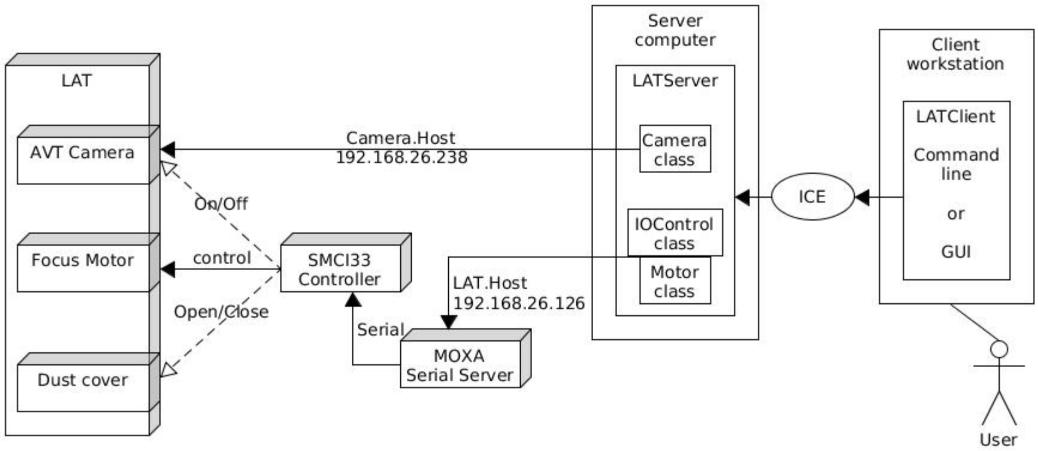

Figure 6.1: UML deployment diagram of the LAT Control software. Note that the client side can be any software over the network that implements the LAT Server ICE interface, including ARGOS or general LBT users.

6.1 UML Diagram

Prior to programming the control software (LATControl), a design phase was first undertaken. This involved deciding what actions the software will be able to perform and how users would be able to command it. For this, we were inspired by the Unified Modeling Language (UML), a development tool commonly used in the field of software development, to construct a deployment diagram (see figure 6.1) that roughly models the physical configuration of the LATControl system. The UML was also later used to construct a class diagram for our control software (see figure 6.2, and activity diagrams for the various steps in the SLA (see figures 10.4 and 11.2).

6.2 Hardware Communication

Looking at the UML diagram, we start on the left side with the three controlled hardware components that make up the LAT (AVT Camera, Focus Motor, Dust shutter).

6.2.1 Focus Motor

The stepper motor attached to the focus adjustment is controlled by the motor controller which accepts simple text commands over a RS-485 serial interface (see Appendix). In order to remotely send commands over the LBT network, we communicate to the controller with the SDS which has its own dedicated Internet Protocol (IP) address (192.168.26.126) on the LBT network. The SDS then receives the motor commands over a Transmission Control Protocol (TCP) socket connection from the software and passes them onto the serial connection to the controller.

The controller also includes several low-voltage digital outputs that can be set to on or off by updating the input/output (I/O) status of the controller. This is done by sending a string of bits with a 0 or 1 at the positions dedicated to the specific outputs. These digital outputs are connected to relay switches that switch on and off the power to the camera and the dust-shutter valve.

6.2.2 Camera

In order to communicate with the camera, the device is connected to the LBT network with an Ethernet cable and also assigned its own unique IP address (192.168.16.238). This IP is then used by the software to locate and assign a control handle to the device.

Power is supplied over the relay switch controlled by a dedicated digital output located on the motor controller.

6.2.3 Dust Shutter

The hydraulic valve for the dust-shutter is controlled by supplying power to extend the arm and open the door and cutting power to contract the arm and close the door. This power comes from the relay switch controlled by another digital output located on the motor controller.

6.3 LATServer

The control software works on the client-server model in which we have a host computer acting as the server with one instance of the hardware control service and its constituents (see figure 6.2) running while multiple instances of clients across different end systems (including from the server computer itself) can access the control service with commands. We implement the server side with the LATServer program written in the object-oriented C++ language. This creates an instant of the LatI class, itself an implementation of the Internet Communications Engine (ICE) framework LAT base class that packages the camera drivers, motor commands, and I/O status updates into three abstract classes and calls their accompanying functions. ICE and its reason for choosing it will be detailed in the next section.

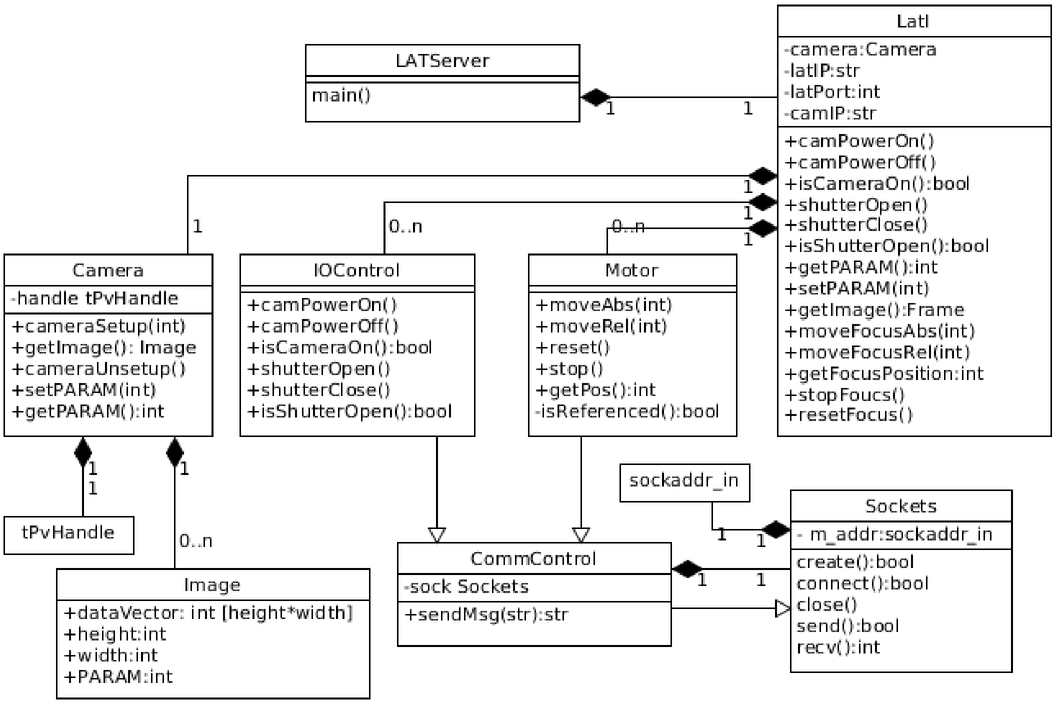

Figure 6.2: UML class diagram of the LAT Control software and its various dependencies. Note that LATServer is the C++ program that will run on the LBT computers and that users can call the various LatI functions using their own programming language, thanks to ICE.

6.3.1 Camera Class

AVT provides two versions of its application program interface (API) to control the cameras it manufactures: the newer Vimba and the older PvAPI. Despite the recommendation of the former by the company, the latter was chosen due to the advantage that more examples are available in the open-source community and the libraries are already stored in the ARGOS source repositories.

The AVT camera allows image capture in both 8 bit depth or 12 rescaled to 16 bit depth. The latter was chosen and set as default because the added depth could give better Gaussian fits over lasers for the SLA (see section 10.2).

The PvAPI is then implemented by the camera class first opening the camera with a cameraSetup() function via its Internet Protocol (IP) address over a TCP connection and then pointing a member variable handle to the camera. Further functions can then be called on this handle with the camera object including setting the configurable parameters (exposure time, horizontal and vertical binning), setting the camera to image capture mode, taking an image and returning it as a vector of CCD counts, and of course closing the camera control (see figure 6.2).

6.3.2 CommControl Class

As the motor and I/O status updates both involve communication to and from the motor controller over the SDS, a single CommControl class was created that derives its base TCP socket communication functionality from a Sockets class provided by Jose Borellli of the ARGOS team. This CommControl holds a key function that sends custom text string communication to the motor controller. It is this function that is used with specialized string and integer sequences by the next layer of derived classes, Motor and IOControl, to control the motor and turn on and off the camera and dust-shutter relay switches.

6.3.3 Motor Class

A simple task such as moving the focus motor a number of steps away from the LAT involves sending a series of simple commands to the motor controller over the SDS. This includes setting the motor to relative movement mode, setting the direction of motor movement, setting the number of movement steps to take, and finally starting the motor. We bundle all this into a simple RelMove() function that takes in an integer with a sign indicating away from the LAT in the direction of the end switch (positive) and towards the LAT in the direction of home (negative). We also implement this layer of abstraction for other motor controls such as absolute movement with a specific motor step position, resetting the motor to home, calling an emergency stop to all motor movement and asking the current limit switch status from the I/O status (see next subsection).

Note that we implement a step limit in the software of 9000 steps to avoid triggering of the end switch which sits a couple hundred steps above this. This prevents unnecessary position errors that the motor controller sends if that switch is triggered by users requesting an absolute or relative movement that would move beyond it. This means if a step position returned by the controller is ever above 9000 or under 0, the motor is not properly referenced and should undergo a home reset.

6.3.4 IOControl Class

The motor controller contains a 32-bit bitmask that encodes the status of the various digital inputs and outputs. For example, the first two bits are the inputs for triggering the limit switches on the camera side and LAT side respectively. When one of these switches are triggered, the respective bit is marked to a 1 for on. Similarly, the digital outputs for the dust-shutter and camera power relays are assigned to bits 16 and 17 respectively.

As an example, if all other bits were set to 0 (the camera and dust-shutter valve were both off) and we asked the motor controller for the I/O status, with both limit switches triggered, we would receive a 32-bit integer with a 1 as the first and second bits and 0 in the rest. This would be a binary number of 11 with thirty zeros in front of it, giving us a 3 in decimal. We can then extract the bitmask information from this 3 by using the bitwise operators that C++ provides.

So, by reading this bitmask using the motor controller's I/O status command, we get a 32-bit integer that contains the information about these individual bits. We then use bitwise operations that allow both the translation of the integer into the status of the bits received from the controller and, conversely, the creation of an integer with certain bits activated and deactivated to send to the controller. By using the former, we can get the status of our limit switches for the previous Motor class and for this class to check if the camera or dust-shutter valve are on or off. The latter can be used to send integers to activate or deactivate the dust-shutter and camera relay switches. It is the capability of the latter that we package into an IOControl class that provides the functions to open and close the camera in addition to turning on and off the camera (see figure 6.2).

6.4 Ice Interface

The classes above are instantiated as objects by the top layer LatI which is then itself instantiated by the final LATServer program. LatI stands for LAT Implementation, which brings us to the client-server layer of our software. As mentioned before, we use the open-source ICE framework as a key component of our control software. ICE allows us to generate a LAT class using its own programming language, slice, that contains its own set of functions that we want a user to be able to call in order to control the LAT hardware. After the desired callable classes and functions are written in slice, we can then generate a Lat object in any language we choose. Using the chosen language, we then need to write a server that implements the action of the functions written in slice; in our special case we wrote the C++ LatI class.

Once the server is up and running with the implemented ICE Lat object implemented, multiple clients can then connect and call the various functions of our C++ server using their own languages of choice. This is a great advantage to have with the LAT, because as a general use instrument on the LBT, we want anybody to use the running LATServer with flexibility. If a user wants to use the LAT, he or she can write a client program in C++, C#, Java, JavaScript, Objective-C, PHP, Python, or Ruby, proceed to generate a Lat ICE object using a slice conversion tool, and implement it in a client program to gain full functionality of the LAT.

6.5 Test Client

In order to test the functionality of the LATControl system and LAT hardware, a simple test client program was written in C++ that can be run from the Linux command line (CL). The client works by executing the LATClient program while including arguments that are parsed and read to execute different LAT controls. Please see chapter B in the appendix for these test client arguments.

7 Installation

7.1 Testing

7.1.1 Prototype

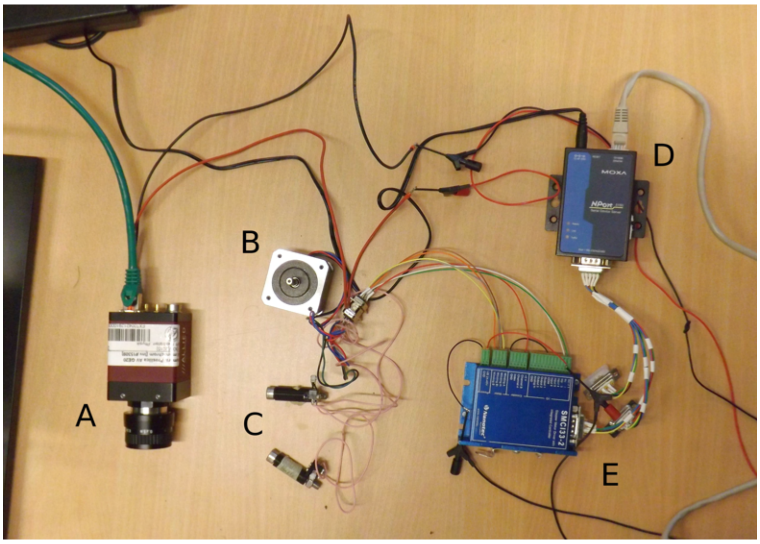

Figure 7.1: ProtoLAT with most hardware components minus dust-shutter and telescope in working configuration. A: AVT Camera, B: Focus stepper motor, C: Limit switches, D: MOXA Nport, E: Stepper motor controller

Prior to full assembly and installation, a prototype of the LAT (ProtoLAT) was configured upon with which the software would be tested (see figure 7.1). This set-up could be run alongside the LAT with the camera attached for near full emulation of the final LAT. The only missing component until final housing assembly was the hydraulic dust-shutter, however since the opening and closing fully rests with a digital output on the motor controller, the software testing could function without it.

The Haus der Astronomie across from the MPIA kindly lent an extra Celestron Advanced VX Mount to the project. This heavy-duty semi-professional equatorial mount benefits from a multi-star electronic calibration system for accurate tracking. To get test images of the ARGOS lasers that appear true to the final images once the LAT is mounted on the LBT, it was critical that the equatorial mount have its embedded tracking computer calibrated to several stars, its polar axis aligned to the celestial pole, and its counterweight and LAT position balanced so the motor does equal work in whatever direction it is moving the LAT in right ascension (RA) or

Figure 7.2: Initial calibration and testing of ProtoLAT with the Celestron mount on the roof of the MPIA. Note that the counterweights attached to the chrome bar on the left side can are adjusted in addition to the LAT position's on the mount in order to achieve balance for more precise tracking of the celestial sphere.

declination (Dec). The first two required a process in which the mount was aligned as parallel to the meridian as possible. Using a local star chart, the LAT would then be manually aligned with the most easily recognized stars and programmed into the calibration system.

7.1.2 Balancing

The weight balancing could be done by directly measuring the power consumed by the mount when varying both degrees of freedom in RA and Dec. We first inserted an ammeter between the required 12-volt power supply and the power port of the mount (see figure 7.3). Then, using the power equation to relate power(P), current(I), and voltage(V),

$$P = I * V$$

we found that if we hold a constant voltage of 12-volts from the power supply, we

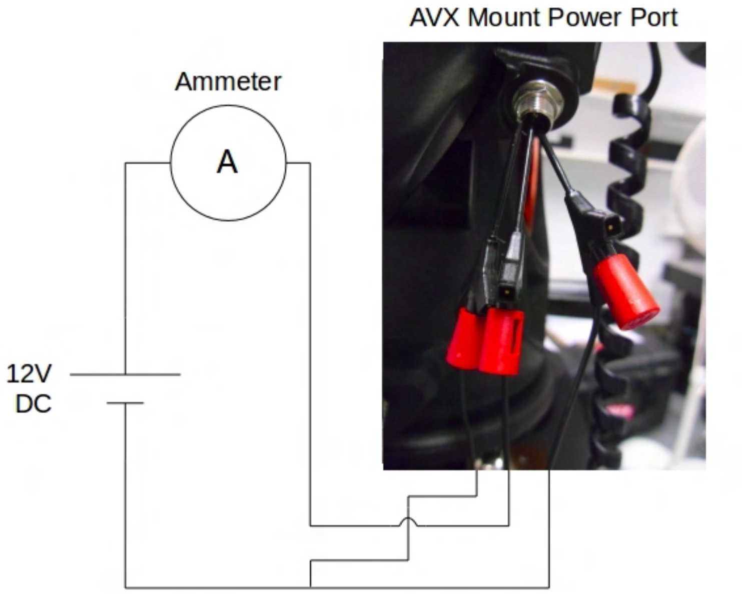

Figure 7.3: Circuit diagram showing the DC power supply running its positive line through an ammeter and ultimately to the inner node of the AVX power port. Two clamps then come off the outer and an inner metal nodes to attach back at the negative node of the power supply.

could assume a balanced mount when either direction on both degrees of freedom drew the same amount of current from the power supply. The counterweight and LAT position had to both be quantified and marked as they were often removed from the mount for easier transportation to and from the roof of the MPIA and the top of Mt. Graham in Arizona. We quantified the counterweight position for RA balance as the distance from the base of the counterweight bar (see figure 7.4a) with both weights pressed together. The LAT position for Dec balance was quantified by the distance from the camera end of the main tube to the first transport hand clasp (see figure 7.4b).

Arbitrary positions for the counterweight and LAT were chosen and the motors were both moved back and forth with currents recorded until both directions for the particular degree of freedom drew the same amount of current through the ammeter. After several adjustments of the counterweight and LAT, the final positions were found as 8cm for the counterweight position to balance RA and 27.5cm for the LAT position to balance the Dec (see figures in 7.5).

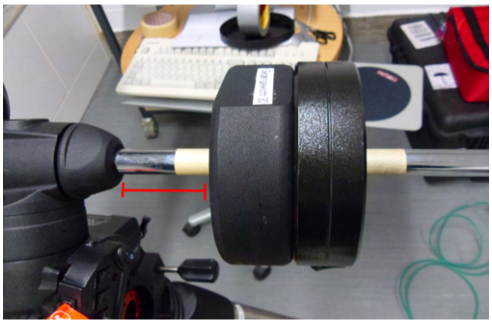

(a) Counterweight position in red. This was adjusted to balance the mount's RA movement

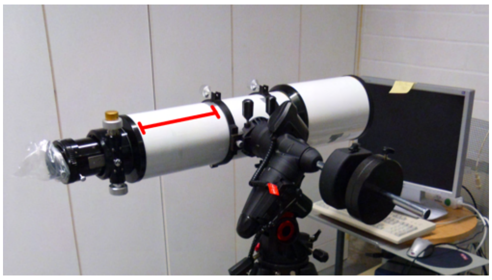

(b) LAT position in red. This was adjusted to balance the mount's Dec movement

Figure 7.4: Quantified adjustment distances for the RA and Dec balancing of the AVX mount

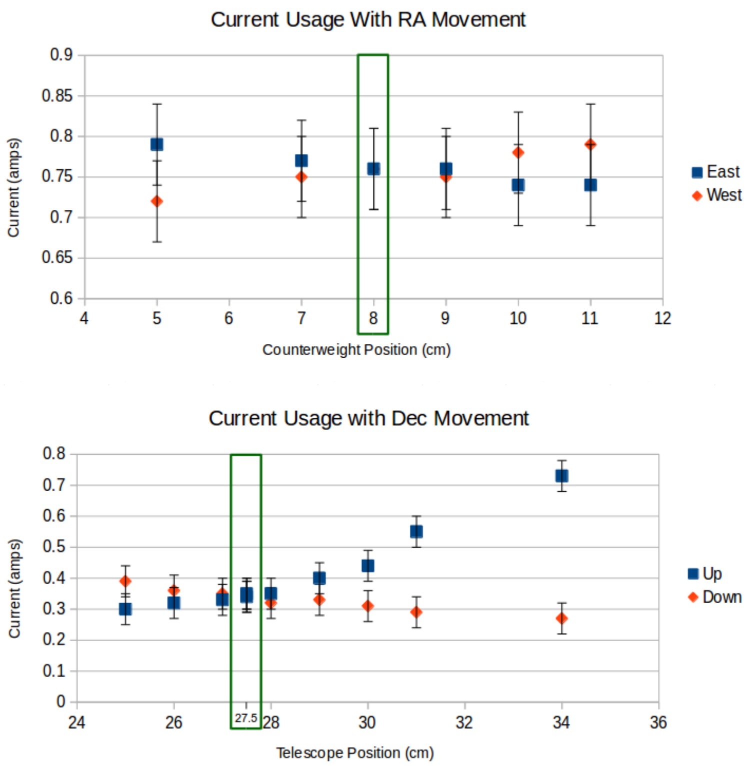

Figure 7.5: Plots of current readouts from ammeter as balance adjustments were made. The green boxes indicate where the final positions were set for both degrees of freedom

7.1.3 Focal Length

With a properly balanced LAT-mount setup, an attempt was made to roughly find at what distance the focus position has to be set for the camera CCD to be at the focal point of the LAT. This would provide not only a good point from which to start the focus position when fine-tuning for taking quality laser images, but it allowed us to establish familiarity with the ProtoLAT before testing on-site at the LBT. The ProtoLAT was set up on the roof of the MPIA and multiple images were taken of bright stars (Vega and Arcturus) over several focus positions using the engraved distance measurements on the focus tube (see figure 7.6). Several images were taken and stacked at focus positions near where the stars appeared to have the smallest radius (see figure 7.7).

Attempts were made to quantify these radii with Full width at half maximum (FWHM) calculations of 2D Gaussian fits or edge to edge measurements, after which a curve with positive concavity could be fit to find where the radius would reach a minimum, thus indicating the actual focal length of the LAT. However, these attempts failed and a clean curve could not be found from which to estimate the true focal length, as we can see in figure 7.8. This was assumed to be due to optical aberrations in the LAT itself that will be touched on in chapter 17. We proceeded to estimate from the images in figure 7.7 a rough position for the true focused position of the LAT. We chose between 5.2cm and 5.3cm as this seems to concentrate the flux from the star into the smallest area.

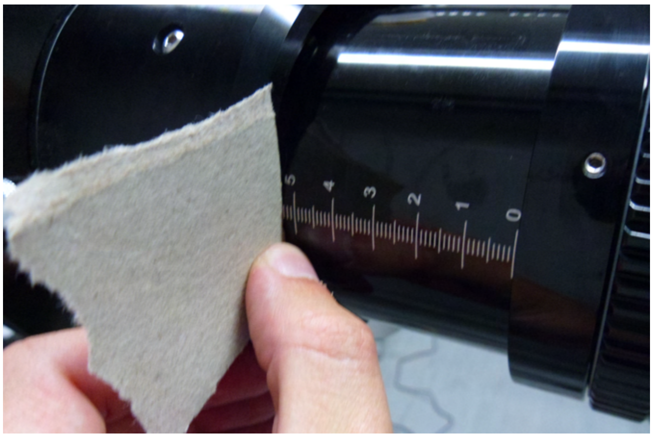

Figure 7.6: Method for measuring the focus position involved using flat piece of cardboard flush with the main LAT tube end to assign a position on the engraved scale. This position is defined as the "focus position".

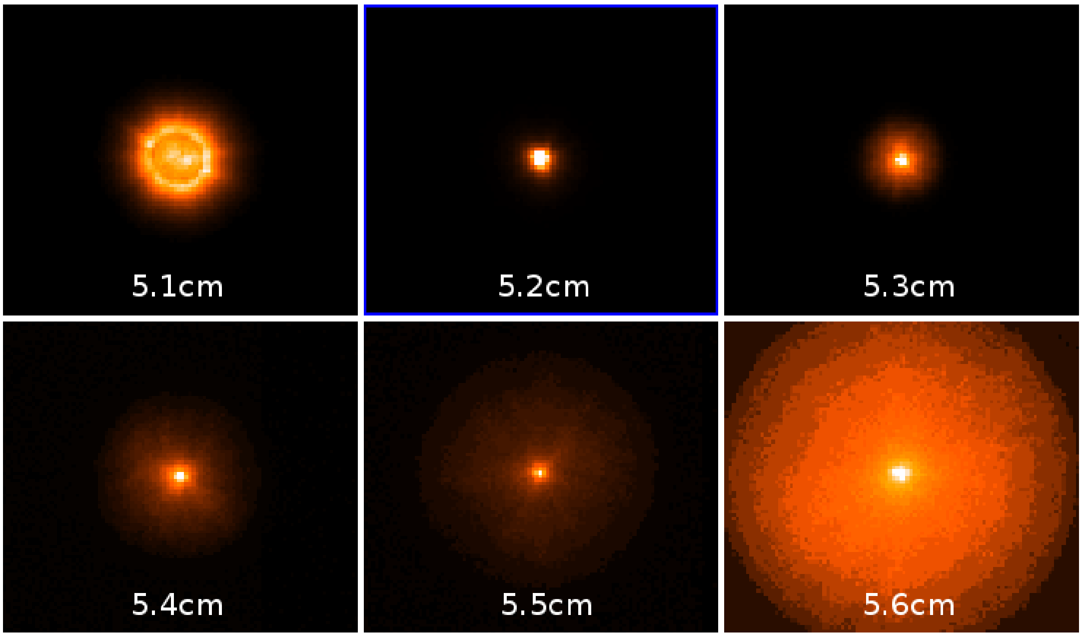

Figure 7.7: Stacked LAT images of Arcturus at various focus positions. From 5.1cm to 5.6cm, the size of the bright center of the star seems to decrease twice, as confirmed in figure 7.8. We roughly estimated 5.25cm as an acceptable position to focus the LAT camera.

7.1.4 Initial Laser Acquisition

The next step in the testing phase was to acquire adequate laser images upon which the future SLA algorithm could be tested. Previous images taken from the MAT-WF were available which provided a certain degree of comparison to the potential LAT images, but the resolution and bad pixels encouraged the acquisition of LAT images as soon as possible. It was on the first commissioning run at LBT with the ProtoLAT and a primitive LATServer where the first laser images were to be obtained. Due to the tracking of the LBT and ARGOS lasers with the celestial sphere, the familiarity with mount calibration and balancing done in subsection 7.1.2 was essential.

To view the maximum amount of sky while having a clear view of the lasers, a few locations around the LBT were considered to position the ProtoLAT. After consulting the ARGOS team for the list of reference targets for the laser commissioning and scouting out the potential tests sites in person, the final observing location was decided on shown in figure 7.9. This location offered the best trade-off between view obstruction from trees or the LBT itself and visual access to the chosen targets for the night.

The first LAT images of the lasers were then captured. As predicted, there was only one night for this commissioning run and it was short, so further laser pointing scenarios would need to be simulated through direct image manipulation. During this test commissioning run, effort was also taken to find an acceptable exposure time for

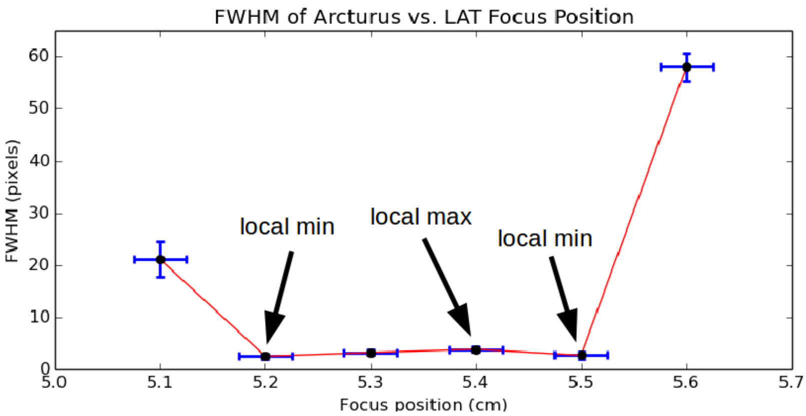

Figure 7.8: Here the median of the calculated full width at half maximum (FWHM) along both major and minor axes of the fitted 2-dimensional Gaussians of Arcturus were extracted and plotted against the LAT focus position (see figure 7.6 for position definition). Note the local maximum at position 5.4 cm and two local minima at position 5.2cm and 5.5cm. The two local minima suggests astigmatism with the telescope that will be discussed in chapter 17.

Figure 7.9: Satellite view of LBT with potential LAT testing locations marked out in X's. The final chosen location is colored green.

the camera. Since we are using the 12-bit depth of the camera, a saturated pixel would hold a CCD count of 4095. Therefore in order to keep LAT images comfortably in the linear regime, we tweaked the exposure time until the pixel with the highest count fell under half of the maximum possible. This occurred with an exposure time of 200ms. By keeping the CCD in the linear regime, we can be more confident later when calculating actual photon counts for height analysis (Howell et al. [2006]).

With the first laser images taken, a series of scenarios had to be considered of how lasers could be oriented in an LAT image. For simulating the new images, see section 9.

Figure 7.10: One of the first laser images captured by the ProtoLAT. Note that the ARGOS lasers are pulsed at a rate of 10kHz, allowing an exposure time of 200ms to image the laser as a solid beam.

7.2 Assembly

The assembly of the LAT was done in several stages. The first was the machining of housing parts done at the Max Planck Institute of Extraterrestrial Physics (MPE) in Garching according to the outsourced plans. Next was the assembly of the housing along with the fitting of the LAT, also done at the MPE. The complete LAT was then shipped to the MPIA for final hardware and control software testing before being sent off to the LBT.

7.3 Mounting

Mounting of the LAT onto the LBT took place on the second commissioning run two months after the first. It was done over several days to remove the MAT and manufacture a custom mount for the LAT before bolting it on the the SX C-ring extension of the LBT (see figure 7.11). The electronic box is mounted nearby so all control relies on the LATServer in the control room. Engineers from the MPE were primarily responsible for this phase while we ran on-site tests of the LAT control software over the LBT network.

(a) MAT prior to removal. Note the MAT-NF is the smaller telescope in the bottom right and MAT-WF is the bigger telescope.

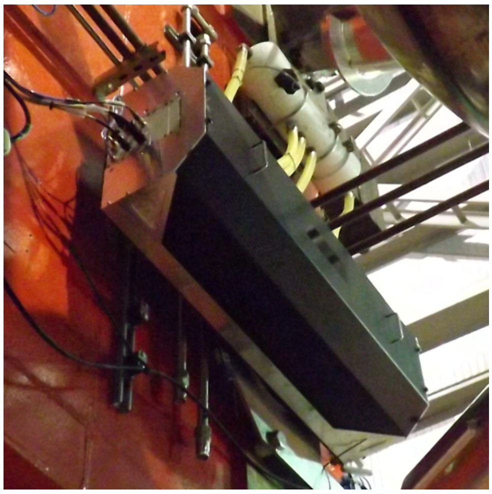

(b) LAT in final mounted position with cover in place

Figure 7.11: Replacing the MAT with the LAT

7.4 Alignment

With the LAT mounted, the next step was to align it with the LBT optical axis so that the center of the captured images would correspond roughly to where the LGSs should be aligned with the ARGOS wavefront sensor. To do this, the LBT would first align its optical axis in the direction of a chosen celestial target. An image was then taken with the LAT and the distance in pixels between the center of the image and the target was calculated. The pixel offset then had to be converted to a millimeter adjustment on the alignment indicators of the LAT. The conversion involves simple trigonometry along with the LAT pixel scale. First the CAD model is needed to measure the sides of the triangles formed with the alignment indicators and pivot axes (see figures 7.12a and 7.12b).

This would give us angles for altitude and azimuth, but to finally convert to pixels, we also need to invoke the 1.7" (or 8.24 μrad) pixel scale of the LAT. In the end we have the conversion from the required alignment indicator adjustment in millimeters (d_{alt} and d_{azm}) to desired pixel change on the LAT CCD (p_y and p_x):

$$d_{alt} = \pm 326 \tan(8.24 * 10^{-6} p_y)$$

$$d_{azm} = \pm 369.9 \tan(8.24 * 10^{-6} p_x)$$

But what about the signs? To find these, we take the knowledge that both indicators go positive when their stems are pressed in by turning their respective differential screws counter-clockwise. Turning the altitude differential screw clockwise pivots the front of the LAT upward and turning the azimuth differential screw clockwise pivots the front of the LAT to the right. If we also take the fact that the maximum pixel offset we could have is 2048, we get a maximum possible angle on the order of 10^{-2} radians within the tan(), so we can make the approximation $\tan(x) \approx x$. Therefore in the end we have a conversion between CCD pixels and indicator millimeters of:

$$d_{alt} = -2.69 * 10^{-3} p_y \tag{7.1}$$

$$d_{azm} = -3.05 * 10^{-3} p_x \tag{7.2}$$

with counter-clockwise screw adjustment causing positive indicator change in millimeters. This also gives us a precision measurement for our manual tip-tilt adjustment of the LAT. Since our distance indicators are precise down to 0.01mm, the two equations above tell us that we can align our LAT to within 3.7 pixels in the y-direction and 3.3 pixels in the x-direction.

This alignment was done several times with several targets due to fine-tuning of the above equations and confusion over the differential screw adjustment directions. One of the iterations with HIP 7232 will be offered as an example.

In figure 7.13 we see that the center of the LAT is off by 84 pixels above in altitude and 262 pixels to the left in azimuth, so alignment must be changed by -84 pixels in y direction and +262 pixels. By equations 7.1 and 7.2 we get alignment indicator adjustments of 0.23 mm for altitude and -0.80 mm for azimuth. The signs indicate that the altitude screw would need to be turned counter-clockwise and the azimuth clockwise.

7.5 Flexure Model

From the beginning we expected the center of the LAT FOV to undergo a varying offset from that of the LBT over the range of elevation (altitude) angles of the LBT telescope. This would come from flexure in the metal housing of the LAT in addition to varying tension being applied to the tip-tilt springs. However, it was not clear how much this offset would be and whether it would be important to consider in the later SLA algorithm. If the center of the LAT FOV varied over more than 30" from that of the LBT from the low elevations (45 degrees) to zenith (90 degrees), then our algorithm would not be able to align the lasers to within the FOV of the patrol cameras. This called for a flexure model to be calculated early on.

At the end of the first night after alignment, a series of targets were aligned along the optical axis of the LBT and a LAT image was taken. Using the process described in the previous section, the pixel difference between the center of the LAT CCD and the intended target were then recorded and plotted in figure 7.14. The extracted

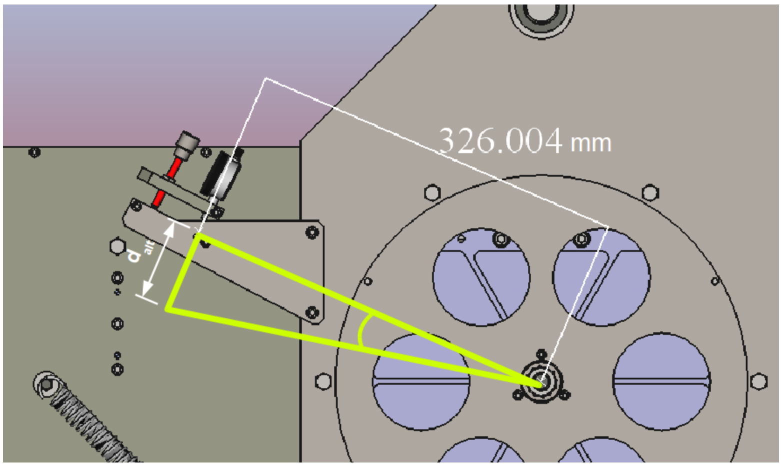

(a) Underside view of CAD LAT housing model with 326 mm measurement of triangle side for altitude adjustment

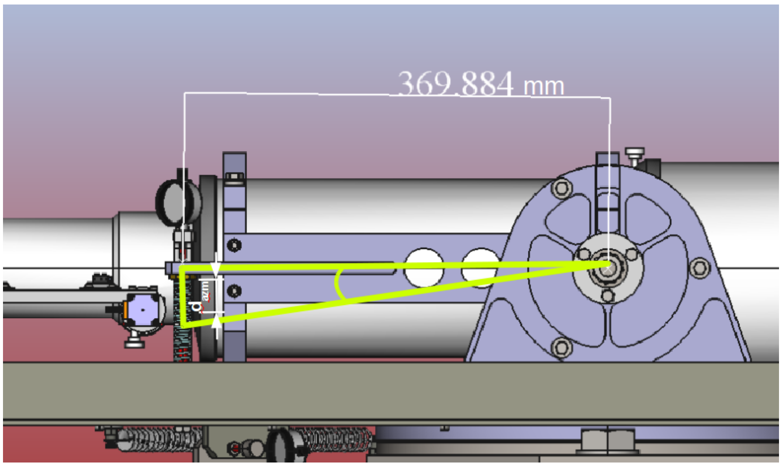

(b) Side view of CAD LAT housing model with 369.9 mm measurement of triangle side for azimuth adjustment

Figure 7.12: Triangle measurements from LAT housing model to convert from angle on sky to distance tip-tilt adjustment

slopes of the lines reveal how much the LAT flexes as -1.16 horizontal pixels and 0.448 vertical pixels per positive degree tilt in LBT elevation. Another interesting feature of the plot is where the two linear fits intersect around 0 pixels, or where the center of the LAT CCD lies directly along the optical axis of the LBT. This is around 76 degrees, which happens to be the elevation where the final alignment procedure took place, suggesting the procedure described in figure 7.13 is reasonably precise.

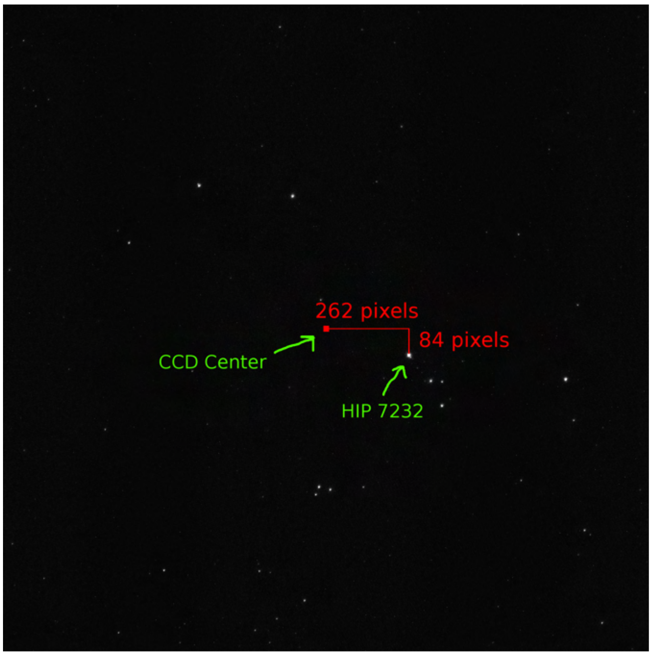

Figure 7.13: LAT image taken with LBT optical axis centered on HIP 7232 in M103. Pixel offset from LAT CCD center is calculated. Note for LAT alignment: the y-axis is inverted.

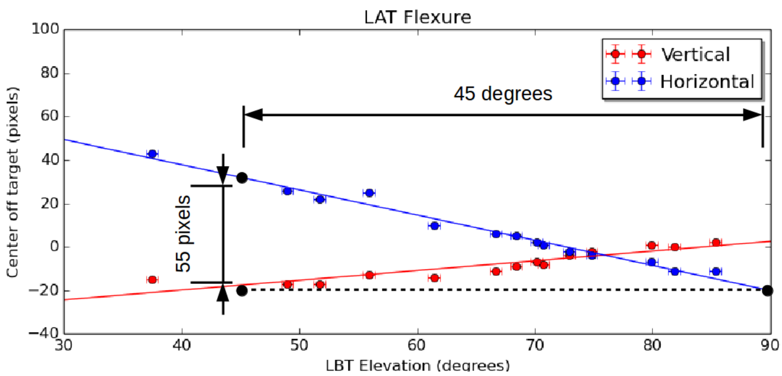

Figure 7.14: Plot of data points for LAT Flexure Model. Horizontal pointing deviates by -1.16 pixels and vertical pointing deviates by 0.45 pixels for every positive degree change of the LBT. Note that over the laser operating elevations (45 to 90 degrees), the LAT pointing can deviate by up to 55 pixels or more than 90" in the horizontal direction. This is well above our 30" error budget, requiring flexure compensation in the SLA.

Part III

Smart Laser Alignment Algorithm

8 Smart Laser Alignment Algorithm

After the LAT was built and installed on the LBT, the focus of the project could turn towards the second part of the project of developing an algorithm to align the 12km points of the lasers with the ARGOS wavefront sensors.

When we take a LAT image of the lasers, there are two ways we can proceed. The first would be to find the points on the CCD along all three lasers that correspond to 12km on each beam. We can then try to align these with where we estimate the wavefront sensors point on the CCD. There is an issue with this in that we do not have a straight-forward method of locating these 12km points. We can attempt a Rayleigh scattering model, but after that, we still run into the issue of finding where the wavefront sensors are pointing!

The second and simpler method simplifies the problem by locating a consistent point along the beam and calculating the offset with an abstract target that, when overlapped with the endpoints (see figure 8.1), align the wavefront sensors with the 12km points. We can take the ends of the laser beams (where laser light transitions to background noise) as these consistent points.

Recall that we need the 12km points to move to within 30" of the wavefront sensors, from which the patrol cameras can image the beam pulses and pass control onto the ARGOS acquisition system. The task of our algorithm thus involves taking an image of the laser beams from the LAT, distinguishing where either the SX or DX beams are, fitting lines along these beams, plotting the integrated flux profiles along these lines, and finally marking where these profiles reach the background noise level, indicating the laser endpoints. After these are found, we need to define a target that marks where the endpoints have to move in order for the 12km points to become aligned with the wavefront sensors. In addition, we need coordinate transforms from LAT pixels to LM1 mirror degrees of freedom for both SX and DX sides so the ARGOS system knows where to repoint the lasers.

A series of tests and simulation images will also be made to help set a standard of robustness while being able to measure the algorithm speed among different methods of our algorithm implementation. After successful completion of the SLA, it will be integrated into the ARGOS architecture along with a graphical user interface (GUI) that will be primarily built by the ARGOS engineers.

The SLA was written in Python because as an interpreted language, parameters could be easily tweaked without recompiling and results could be interacted with through the iPython terminal, allowing easier examination of results.

The next chapter (9) will describe the process of simulating laser images on which we could test the SLA as it was written. Chapter 10 will go into detail of how the SLA actually locates the lasers in a LAT image and the various strategies we tried in addition to why we decided to choose the one we did. Once we distinguish the lasers, chapter 11 continues the process of reducing the laser beams down to coordinates of laser endpoints on our CCD that we then use with the schemes in chapter 12 to align the LGSs with the WFS. We also briefly show in chapter 13 how the SLA is used within the ARGOS system.

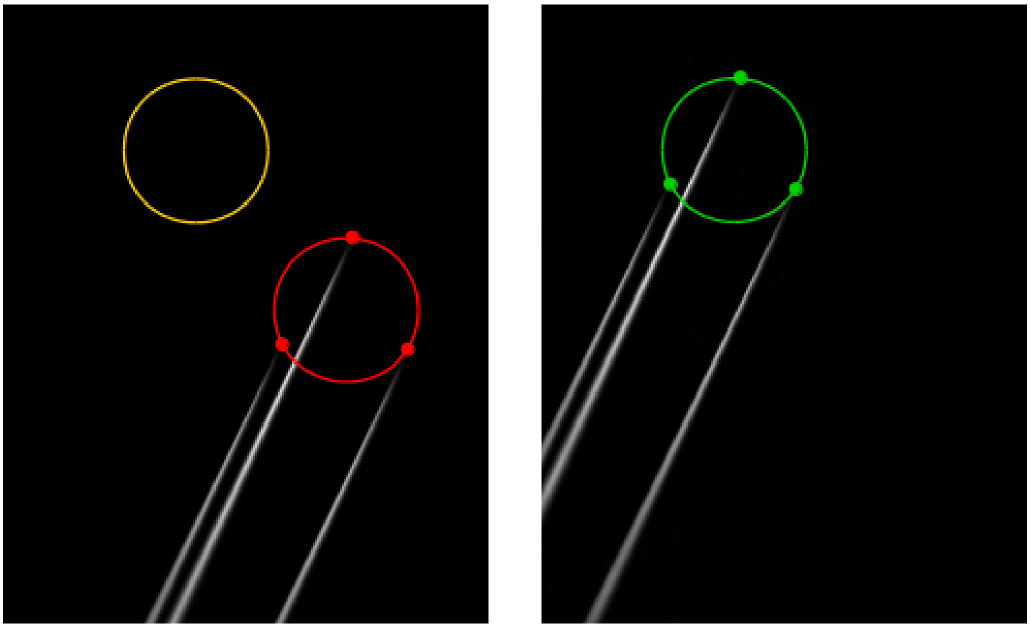

(a) Red circle is laser triplet location. Yellow circle is where we want the lasers

(b) If algorithm works, red meeting yellow would simultaneously align the LGSs with the WFS. Successful alignment is symbolized in green here.

Figure 8.1: Laser alignment plan

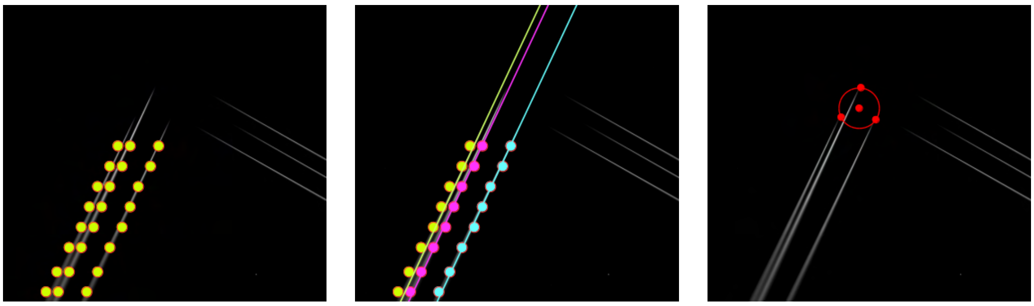

(a) Find laser points

(b) Organize points and fit lines

(c) Use flux profiles along lines and fit circle to end points

Figure 8.2: Laser finding plan

9 Simulated Laser Images

The LAT is located on the front of the left support beam of the LBT, in between the two LM1s. Therefore from geometry we know that to enter the field of view (FOV) of the LAT, the SX lasers would need to appear as lines with positive slopes and the DX lasers would need to have negative slopes. In addition, the first test images revealed that each laser in their respective set of three show very little variation in their slopes among each other and when moved around the entire FOV of the LAT CCD. A random sample taken of a stack of test images taken from the first commissioning run revealed a standard deviation in the slopes of only 0.01. This is reasonable because even though the lasers have a slight difference in angle of about 4', we will be viewing the projected beam on the CDD that extends over about 20 kilometers before scattering as many photons back to the LAT as background noise would, effectively forming an endpoint (Rabien et al. [2008]).

With this knowledge, a set of scenarios was considered out of different configurations the six lasers could take when imaged by the LAT. This included both laser triplets entering from the bottom, both from the corners, both from the sides, and both ending off the CCD. In addition, special cases were considered such as the laser triplets crossing the each other after entering the FOV and before entering the FOV and one with high simulated image noise to cover the early dawn hours for commissioning or observing that extends to the last minute. All the while, the slopes of the lasers entering the CCD were assumed to stay the same.

The master image used for creating simulated images was the LAT image taken of the lasers in figure 7.10. A sky image was also taken by the LAT without the lasers at the accepted focus position (5.25cm) and exposure time (200ms) to function as a background layer. In order to manipulate these fits images to produce the above scenarios, an image manipulation program was needed that not only allowed importing fits files, but would also with 16 bit images. The current stable 2.8 build of the GNU Image Manipulation Program (GIMP) does not possess the latter ability, so it was necessary to use the 2.9 development build which does. The lasers themselves were then cropped out of the master image and placed in the various scenario configurations selected above as new layers over the background image. The result is shown in figure 9.1.

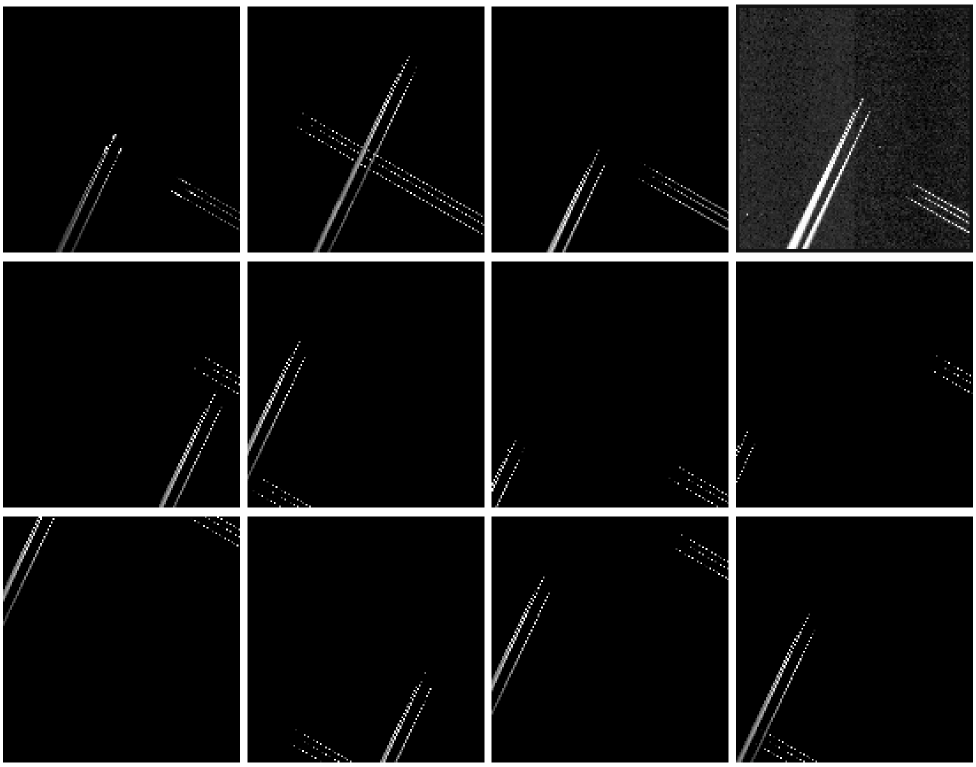

Figure 9.1: Various simulated laser images created with GIMP and the test image in figure

10 Finding Lasers

The actual laser finding can be split up into several steps. The first involves processing the image for analysis. This involves dark subtraction in addition to filtering out most unwanted background noise separate from the lasers. The next step is to then scan the individual rows of the image to "construct" the bodies of each individual laser that the software can categorize separately. Coinciding with this is the validation that each added piece of the laser is assigned to the correct laser. Once each laser is detected and categorized, a consistent point along their lengths needs to be defined that can then be compared to a target position where if the point is aligned in that position, the 12km points of all three lasers are aligned with their respective patrol camera. The actual laser correction is then described in chapter 12.

10.1 Image Processing

To prepare the image for laser analysis, a dark frame was first subtracted to reduce the noise and limit the impact of the few bad pixels. A series of dark images were taken in the early test runs of the protoLAT and stacked to produce a master dark frame. After this is subtracted from the LAT image, an attempt is made to remove most background noise. This is done by calculating a minimum threshold above which CCD counts can be considered laser or bright celestial objects. By assuming a normal distribution with the background noise, this was defined as 3σ above the median of the image. The sigma was estimated simply by taking a random laser image, extracting a region with no lasers, and calculating the standard deviation of the CCD counts (4.5 counts). The 3σ (13.5 counts) above the median we can estimate as containing 99.7% of the noise by the 68–95–99.7 rule in statistics (Devore and Farnum [1999]). All pixels with counts below this threshold are then set to zero as they will not be used in any further calculation when analyzing the lasers. This will speed up integrating the light counts later by having the majority of the pixels in the LAT images equal to zero, though for future height analysis, it should be noted that the noise will still be present in the laser flux itself.

10.2 Identifying Laser Peaks

As we see in the algorithm steps in figures 8.2, we first want to seek out pixels that potentially contain laser and store them. We decided to to this row by row to simplify things. Several methods were explored that seek out and assign potential laser section candidates in each row. Since we want to scan multiple rows, with more rows providing a more accurate final line fit of the laser, the scan should be relatively quick. There should also be a robust tactic to assign each point to their corresponding laser, because afterward we would like to plot a complete integrated flux profile of each laser.

10.2.1 Sideways Threshold Method

The first method we attempted would scan from the left to the right side of the CCD where the pixel counts were measured against a threshold (see figure 10.1). When the scan exceeded and subsequently fell below the threshold after a minimum laser width, the middle point was taken as the location of the laser peak. This was very fast, however the robustness was lacking. Lasers were easily found when the region of search was limited to a custom input by the user, however in order to limit human interaction, it was preferred that the entire image is scanned. When looking through the entire image, the unfocused area of the laser near the base would be highly error-prone due to the lasers blending into one another and therefore not decreasing CCD counts below the threshold. This would in turn cause much of laser base to not be considered when determining the laser direction, which would lead to bad line fits in the final step.

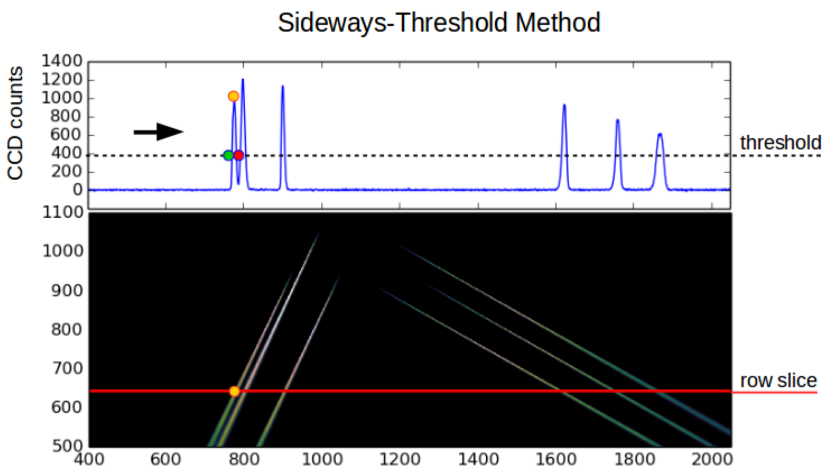

Figure 10.1: Sideways-Threshold scheme finding first laser peak

10.2.2 Skeleton Method

The next method involved first binarizing the image with a chosen threshold, which we initially took to be the earlier mentioned 3σ above the median, effectively making any pixel with counts above the threshold equal to 1 and anything below eqaul to 0. Next the topological skeleton of the image would then be found using the open-source scikit-image library for image processing. Finding the skeleton of an image involves first detecting edges in the binarized image and then reducing the shape to a path with a set width with all points being equidistant from the edges originally detected. The rows can then be scanned and with a simple image like that of our lasers, we should get a nonzero pixel wherever a peak of maximum counts exists.

This method ended up being rather robust as we could have the lasers themselves reduce to simple lines before then scanning where those lines are located (see figure 10.2). However, the skeletonization process took a surprisingly long time. Also, a relatively high threshold had to be chosen a bit higher than the 3σ to binarize the image because of the blurry laser bases again blending into each other. This can negatively impact robustness, especially if there is a situation with a low signal to noise such as with clouds and fog decreasing laser flux or the early dawn hours increasing background noise. Also, it was while exploring this method that we noticed the LAT suffers from a noticeable amount of coma (see chapter 17), which would cause non-symmetric beams. This leads to the found peaks in the row scan to not correspond to the peaks of the lasers, so our later flux integration would lose CCD counts.

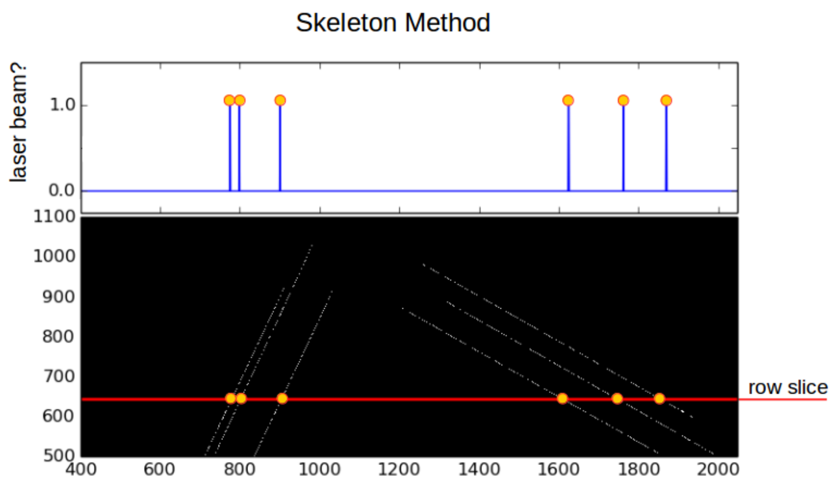

Figure 10.2: Skeleton method extracting row from skeletonized image. Peaks are the 1's in the extracted row

10.2.3 Gaussian Subtraction Method

The final method was to first find the pixel in each row with the highest count, fit a Gaussian around the peak, mark the position and subtract the fitted Gaussian. The process is then repeated until the maximum flux over all pixels in the row reaches below a threshold or 6 Gaussian peaks are found, whichever comes first. The peak locations are then arranged from left to right and returned as a vector of peak positions. A very similar routine used in two-dimensional images for radio astronomy was developed in the 1970s known as the CLEAN algorithm (Högbom [1974]). This process is slightly slower than the Threshold Method, however it benefits highly from being able to seek out beams that blend together as long as their peaks are separate, bypassing the blurry laser-base problem from the other two methods. A visual of this method is provided in figure 10.3.

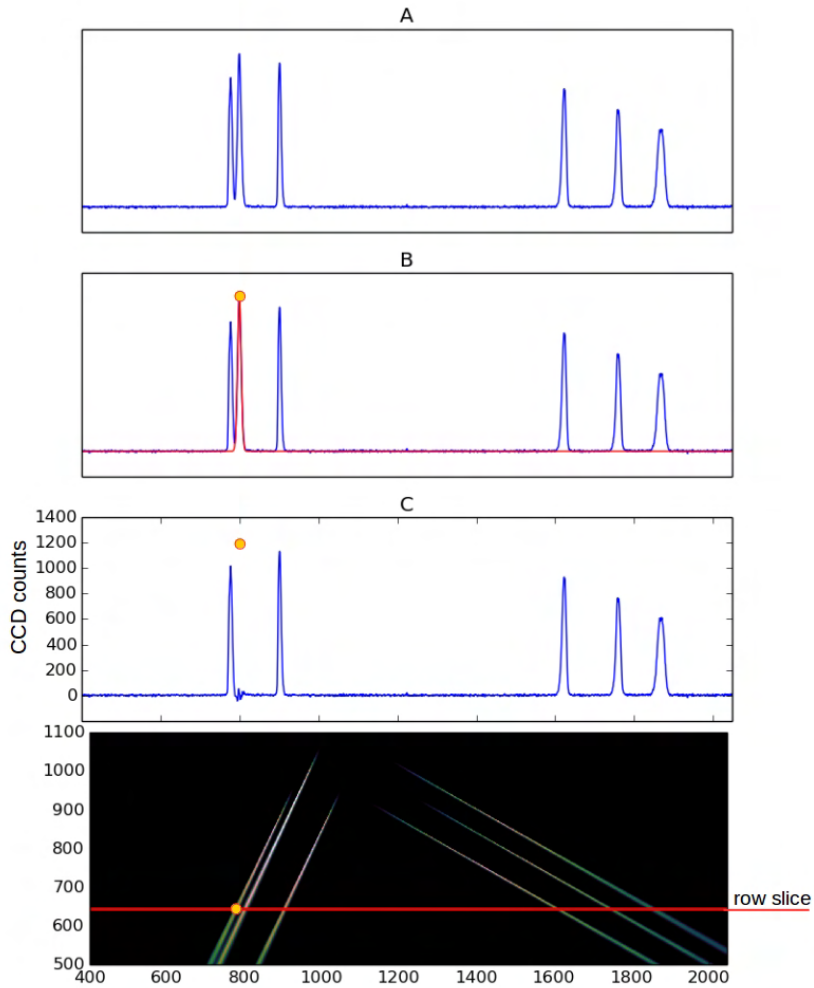

Figure 10.3: Gaussian-Subtraction method in action. Row slice is taken from image, first Gaussian is fitted, peak is marked, Gaussian is subtracted, repeat until six peaks are found or total flux in row is below threshold.

10.2.4 Method Benchmark

A benchmark script was written that runs the full algorithm (see figure 11.2a) with all three methods. Using the collection of simulated images from chapter 9 in addition to more laser images that had been collected during the second commissioning run, the algorithm was run on each image and timed. If the lasers were found with a successful circle fit (see chapter 11, the elapsed time was recorded for the image. The success rate over 50 images was then compared among the methods in addition to the median elapsed time per image (see table 10.1). As the Gaussian-Subtraction method seemed to have the best balance of speed and robustness, we chose it for the SLA.

Method	Time Median (sec.)	Time Std. Dev. (sec.)	Success Rate
Sideways Threshold	2.4	1.2	72%
Skeleton	7.2	1.4	96%
Gaussian Subtraction	4.1	1.5	92%

Table 10.1: Benchmark test of three SLA row scan methods. Time taken for the complete algorithm using the indicated method is recorded alongside the percentage of fits images in the test batch from which all the lasers are adequately located.

We also found planning the steps of the algorithm ideal for building another UML diagram, specifically an activity diagram that outlines the Gaussian-Subtraction method. The result of this planning phase can be found in figure 10.4.

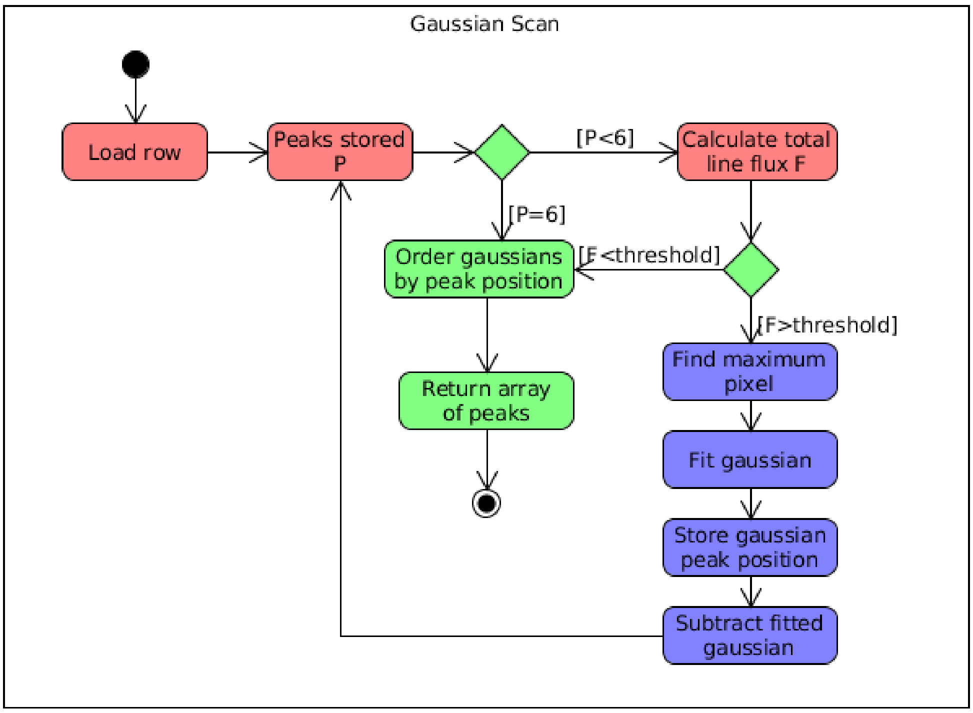

Figure 10.4: Activity diagram of the Gaussian Subtraction method. An activity diagram is read starting at the solid black dot that begins the workflow. The diamonds then show when a conditional situation is reached with different possible outcomes and the workflow is terminated on the encircled black dot.

10.3 Organizing Laser Peaks

For every row scan, a list of potential Gaussian peak candidates is retrieved to distribute among the various lasers. Since the lasers can cross, enter the image at different heights, or leave the image entirely before exposing their ends, distributing the Gaussian peaks is not as simple as assigning them to lasers from left to right (or right to left, if the lasers are crossed!). An extra safeguard is needed to make sure the peaks and their positions are assigned to the correct laser, otherwise the exercise is pointless as the eventual flux profile will not cover the entire laser, or worse, cross multiple lasers. In addition, the finding algorithm should roughly recognize when a laser triplet is finished as it moves up rows, otherwise it could confuse one side's laser peaks as a continuation of the other side's lasers. This last problem is solved by feeding over rows from top to bottom instead of bottom to top as the lasers must always have a base underneath their end points, but there is still the issue of assigning peaks to the correct lasers.

We recall that an important feature was found during initial LAT tests and simulated laser image creation— the lasers in each triplet virtually share the same slope when projected onto the LAT CCD (see chapter 9). This allowed for two possible safeguards, the first to compare the slopes within a triplet and the second to compare the slopes to a stored expected value. The former requires that two or three lasers are present for the laser side being located. As it would be a useful future feature for the system to locate a single laser for testing purposes and the slope of the lasers on their respective sides should rarely change, a stored reference slope was chosen as the preferred organizing safeguard.

As we see in figure 10.5a, in an ideal situation with three lasers and no background objects, we can use our Gaussian-Subtraction row scan to find three peaks and assign the laser peaks from left to right. Now, if we were to move on to the next row and obtain the next three laser peaks, that would be ideal, but as we see in the fitted lines in figure 10.5b, trouble can arise. If there is a bright star in the FOV, as seen in the left yellow fitted line, then it can be mistaken as a laser peak. If the row misses one of the peaks belonging to a triplet because the flux threshold for the row was too high, then the algorithm could assume a laser peak belonging to the other triplet is the correct peak, as seen with the blue fitted line on the right side. However, if we introduced a reference slope for each laser triplet, as represented by the dashed white line in the image, we can make sure the next batch of three peaks lie on the same lasers as the three peaks in the row below them. The image shows this test where the outside two fail with red crosses, but the middle passes. We can then discard this row entirely and move on to the next one, as shown in the final figure 10.5c. Here the next three peaks all pass the slope test and we can proceed to scanning more rows.

Note that this method requires the first three peaks of a laser triplet to lie on the lasers, otherwise even valid peaks in the next row would fail the test. To bypass this dilemma, if only one other row has valid peaks, all of them are removed and the process starts from scratch. Also, we don't test all the peaks with each of the peaks of the previous rows as that would take too much time. Instead, we test the two outer peaks (first and last), the next pair inward (first and second to last), and finally the inner pair (third and third to last). This allows the peaks to be assigned correctly when the lasers are crossed as well because then the SX lasers are on the right side of the CCD and the DX lasers are on the left (see the slope test UML in figure 11.2b).

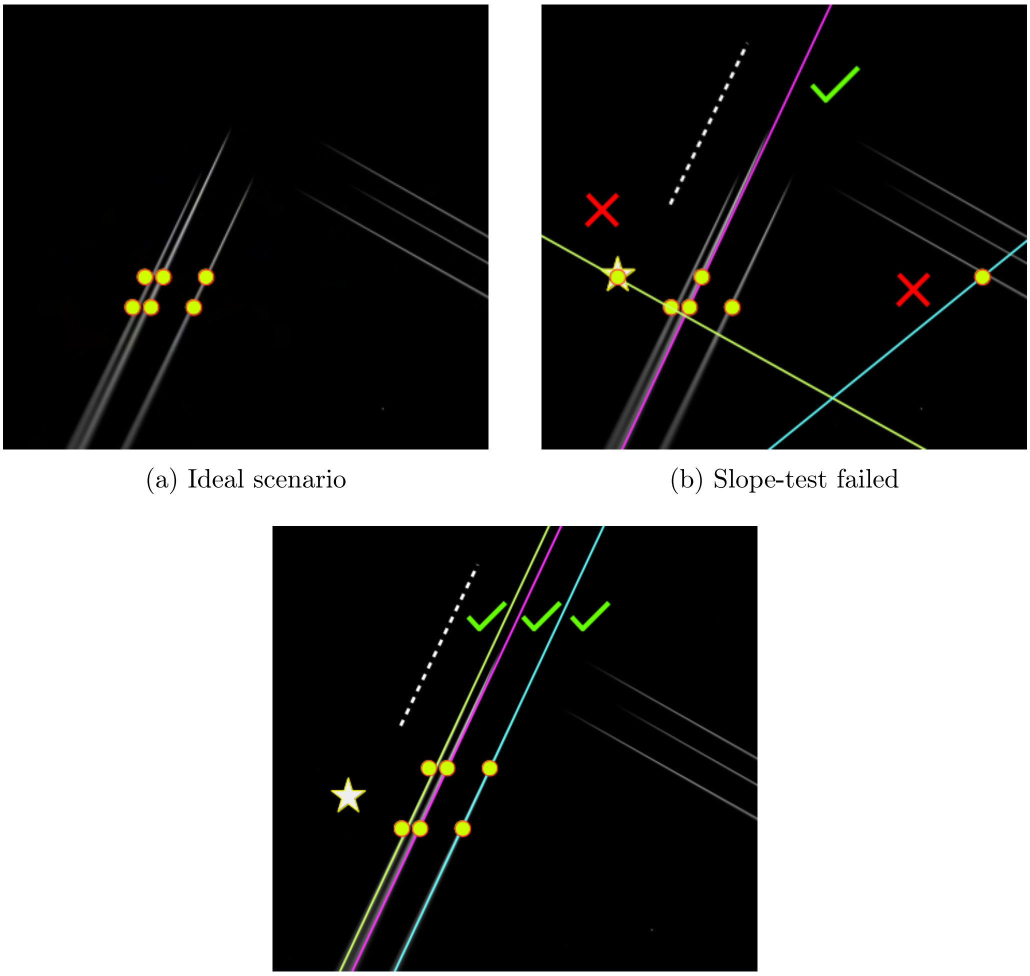

(a) Ideal scenario

(b) Slope-test failed

(c) Slope-test passed

Figure 10.5: Visualization of the SLA with the integrated slope-test.

11 Defining Laser Locations

Once we know how to distinguish the lasers in the image, we need a way to reduce three solid beams to a single pixel that can then be "steered" around the LAT field to align with a target pixel that gets the 12km points along the lasers within 30" of the WFS. From here, users of ARGOS can use the LGS Acquisition system to take over centering the lasers on the wavefront sensor. This will be done by deciding on a standard point on each laser giving three pixels to which a circle of near-consistent radius can be fitted. The center of this circle then becomes the location of the LGS constellation for that side of the LBT.

11.1 Beam Endpoints

As mentioned before, in the LAT images we find quite a high signal to noise ratio for the laser beams. This being the case, we can define the amount of integrated CCD counts along the path of the laser beam where the image transitions from detecting laser beam to purely background noise. Remember the images we are running the algorithm over have been processed to have pixels with only background noise dropped to zero. By plotting the integrated flux profile of each laser and marking where the profile dips down to zero, we have a consistent end point for each laser. As this beam end should exist where the number of photons from the laser is equal to the number of photons detected from background noise, it should be a consistent distance from the 12km focused points on each laser if we assume a clear night. This means we can use the three laser end points from the integrated flux profiles as consistent locations through which a circle can be fitted and whose center gives a two-dimensional location on the CCD. It is this location that we can compare to a target that, when matching, the 12km points line up with the patrol cameras of ARGOS.

The integrated flux profiles were found by integrating the CCD counts along each row over a width of 20 pixels along the fitted laser line. The result is three profiles similar to that plotted in figure 11.1. By marking the coordinates of these three points and fitting a circle to them, we can extract a single coordinate from the circle center. We now have our circle in figure 8.2c. A final UML activiy diagram highlighting this routine in detail along with the rest of the SLA was drafted during the planning phase (see figure 11.2a).

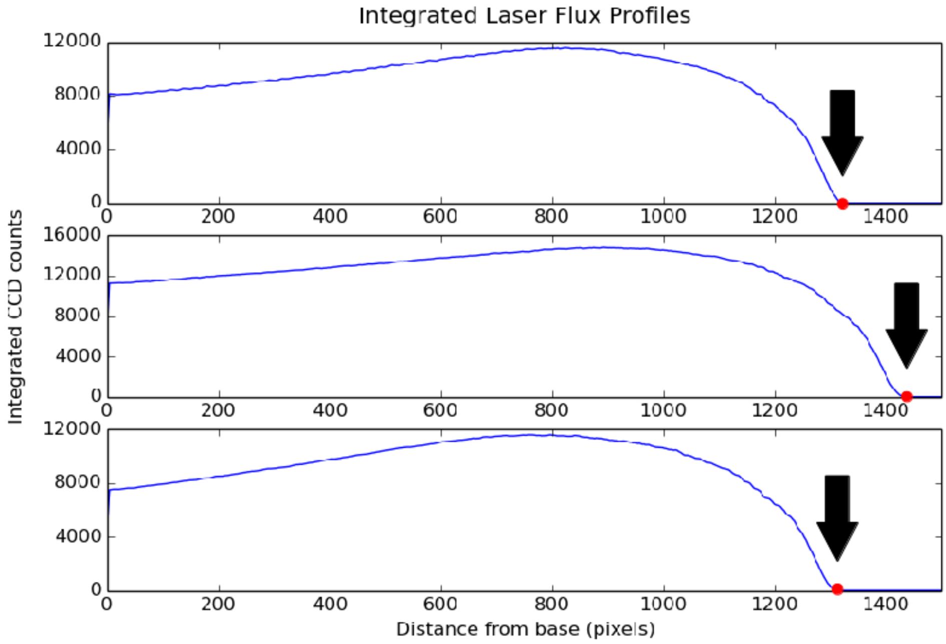

Figure 11.1: Integrated flux profiles of example SX lasers. Where the profiles drop to 0 is where we define our laser end points, as indicated by the red dots.

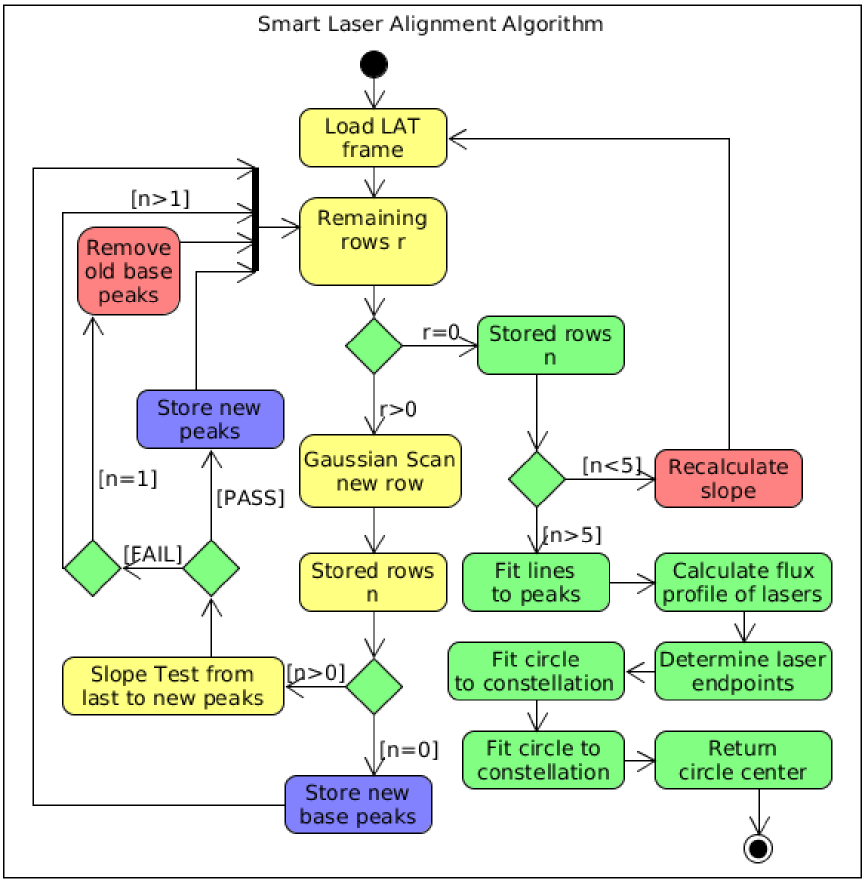

(a) UML activity diagram of the Smart Laser Alignment algorithm. Note the actual aligning takes place after the constellation circle center is returned and compared to the target position as defined in chapter 12

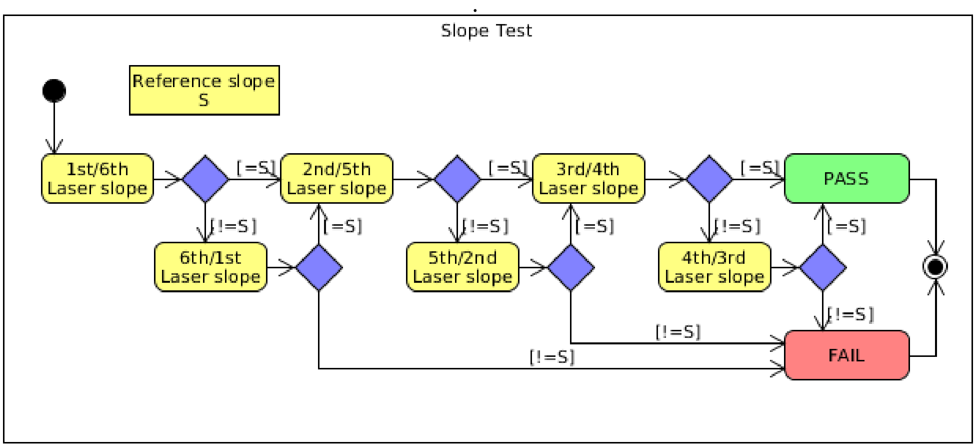

(b) UML activity diagram of the slope-test. Note the first number dictating which laser peak is tested (such as 1st/6th) is when scanning for SX lasers and the second is when scanning for DX lasers.

Figure 11.2: UML activity diagram of the entire SLA with expanded detail of the slope-test activity.

12 Laser Beam Correction

12.1 Calibration

Once the pixel offset between the midpoint location of the lasers and the desired location is found, the lasers themselves need to be moved. There are numerous locations along the laser launch system where the laser pointing can change, but for the LAT we will use the final launch mirrors (LM1) on the back of the LBT secondary mirrors. This mirror has a tip-tilt mechanism controlled by stepper motors that give us the two degrees of freedom, phi and theta, that we need to steer the lasers around the sky. To convert from x and y pixel offsets on the LAT CCD to LM1 phi and theta movements, we assigned both SX and DX an interaction transformation matrix, a strategy provided by Lorenzo Busoni of the ARGOS team.

An interaction matrix (Int) works by first performing an initial two-dimensional calibration between the LAT and LM1. A LM1 calibration offset of a couple hundred motor steps is chosen (we settled for 100) and the LM1 is instructed to take up four positions from an initial home position to complete a cross in the sky. These positions include +100" in phi with 0" in theta, -100" in phi with 0" in theta, 0" in phi with +100" in theta, 0" in phi with -100" in theta, and of course the initial home position. When each of these positions are measured, the SLA is run to locate the laser endpoint circle location in x,y pixel coordinates. The interaction matrix is then defined with the LM1 calibration offset k and initial LM1 position ($\phi = 0, \theta = 0$) as

$$\text{Int} = \begin{bmatrix} x_{(+k,0)} - x_{(-k,0)} & y_{(+k,0)} - y_{(-k,0)} \\ x_{(0,+k)} - x_{(0,-k)} & y_{(0,+k)} - y_{(0,-k)} \end{bmatrix} /2k \tag{12.1}$$

We then take the inverse of this to create a reconstruction matrix (Rec)

$$\text{Rec} = \text{Int}^{-1} \tag{12.2}$$

As long as offsets remain small enough for the transformation to remain valid, we get the resulting transformation between coordinates

$$(\Delta\phi, \Delta\theta) = (\Delta x, \Delta y)\text{Rec} \tag{12.3}$$

The calibration scheme is visualized for both SX and DX lasers in figure 12.1.

We will go through a quick example of the calibration scheme using specific beam end locations found in table 12.1. We take the beam locations for SX and DX and plug them into equation 12.1 to get the Interaction matrix, of which the inverse is calculated as per equation 12.2 to get the Reconstruction matrix. The example results are stored in table 12.2 for each side in addition to the latest calculated Reconstruction matrices that were calculated over several calibration iterations of which the medians of the laser positions were used. Users are advised to use the latter matrices when setting the SLA config file.

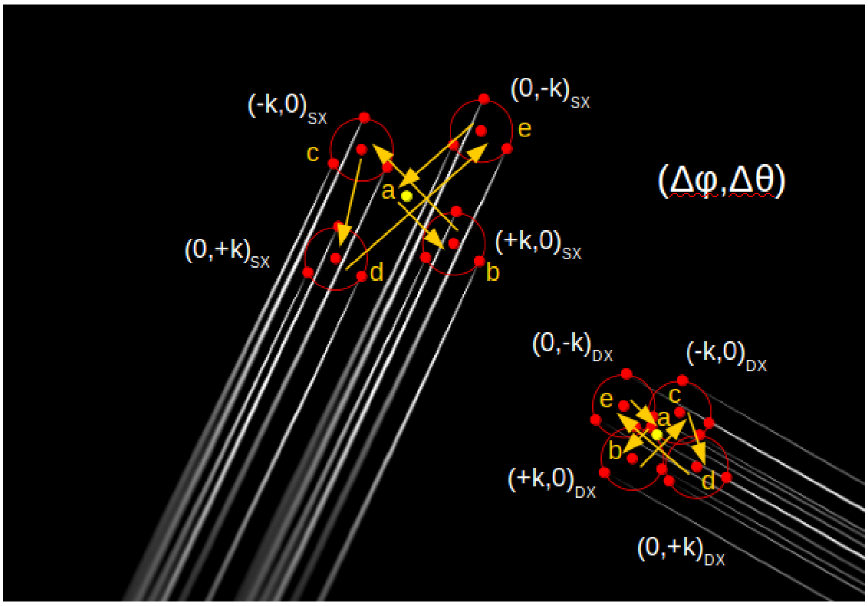

Figure 12.1: The calibration scheme for both SX and DX lasers. The lasers start at a home location indicated by the yellow dots and move through the LM1 coordinate offsets described above while calculating the endpoint locations in LAT CCD x,y coordinates. The results are then entered into equation 12.2 and an interaction matrix is found.

Side	$\Delta\phi$	$\Delta\theta$	x	y
SX				
	0	0		
	+100	0	1101	861
	-100	0	893	1081
	0	+100	831	827
	0	-100	1162	1116
DX				
	0	0		
	+100	0	1426	385
	-100	0	1528	493
	0	+100	1560	367
	0	-100	1397	509

Table 12.1: Calibration data for example run with k=100

SX Reconstruction Matrix (example)	$0.43480877 \quad -0.3309963$ $-0.49799898 \quad -0.31294196$
SX Reconstruction Matrix (latest)	$0.52597931 \quad -0.82471576$ $-0.54451046 \quad -0.72506376$
DX Reconstruction Matrix (example)	$-0.88506607 \quad 0.67314884$ $-1.01595612 \quad -0.63575168$
DX Reconstruction Matrix (latest)	$-0.50560173, 0.83075264$ $-0.54984364, -0.73405369$

Table 12.2: Calculated Rec matrices for each laser side from the example run described above (example) in addition to those calculated with the medians of several iterations (latest). We recommend using the latter matrices.

12.2 Target Position

12.2.1 Error Budget

As mentioned before, we need to get the LGSs into within 30" from the center of the WFSs for the patrol cameras to locate and hand them off to the LGS Acquisition system. Since the lasers are identical in power, they should all three extinguish at the same altitudes, making the endpoints the same distance from their respective 12km points. In addition, as we know from earlier sections that the slopes of the lasers projected onto the CCD have very little variation when moved around the FOV, we can stay confident that the endpoints will always be a consistent pixel distance from the actual 12km points. Thus, if we can align the lasers once manually and use the SLA to find the CCD coordinates of the circle fitted to the laser endpoints, the center of this circle can be the target we enter into the system as the point we want the endpoints to return to when the LGSs are misaligned in the future.

12.2.2 Flexure Compensation

Of course its not entirely that simple. If we refer back to section 7.5, we found there was a significant amount of relative flexure between the LAT and LBT optical axis. Since over the range of the ARGOS operating elevations of 45 to 90 degrees there is more than 30", the target of the laser end points that aligned the WFS and LGSs at one elevation may not align them at another. We need to adjust our end point target to compensate for LAT flexure.

If we refer back to our flexure model in figure 7.14, we take note of the 76 degree LBT elevation around which the LAT CCD center is aligned with the LBT optics. For the target, we therefore store into the system the coordinates of the circle that, when the center of the circle fitted around the three laser ends overlaps with it with the LBT at 76 degree elevation, the LGSs are aligned with the WFS. At other telescope elevations, the difference between the current LBT elevation angle (e) and 76 degrees can be calculated, multiplied by -1.16 for horizontal compensation and 0.45 for vertical compensation and applied to the base target ($x_{\text{base target}}, y_{\text{stored target}}$) to get the new target:

$$\text{new target} = \left[x_{\text{base target}} - 1.16(e - 76), y_{\text{base target}} + 0.45(e - 76)\right] \tag{12.4}$$

The latest base targets found are listed in table 12.3 for reference.

Side	$x_{basetarget}$	$y_{basetarget}$
SX	987	1001
DX	1099	986

Table 12.3: Latest base target coordinates found for SX and DX lasers

13 ARGOS System Integration

With the SLA written, it is up to the ARGOS system to use its own LAT client to take an image, pass it to the SLA from which it receives LM1 coordinates to transmit to the LM1 stepper motors. A Graphical User Interface (GUI) of this processed was constructed by Jose Borelli of the ARGOS team and is featured in figure 13.1.

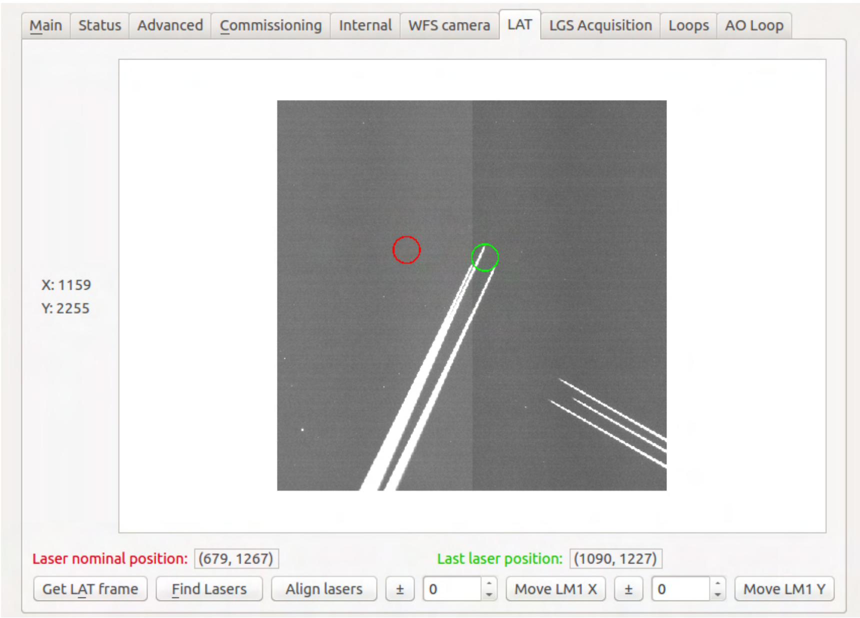

Figure 13.1: Screenshot of the LAT tab of the ARGOS Arbitrator GUI. Starting from the left, we see a "Get LAT Frame" button that simply takes an image from the LAT and displays it with the superimposed laser Target that is calibrated into the system with flexure correction applied. The "Find Lasers" button executes the SLA on the taken image and displays the resultant fitted endpoint circle on the image in addition to its center coordinates. The user can then choose the "Align Lasers" to transform the difference of the Target and laser position into LM1 coordinates using the Rec matrix (also calibrated into the system) and send these to the LM1 stepper motors to apply the laser correction. An added feature was the manual movement inputs on the bottom right that simply use the Rec matrix to move the lasers in x and y directions on the CCD. This is useful for manual laser alignment in the case of a failed SLA.

In addition to a laser alignment GUI, an independent GUI was also created by Jose Borelli that is simply a client for the LATServer. This is simply for basic use of the

LAT and is completely independent of the SLA. A screenshot of the LAT GUI is featured in figures 13.2.

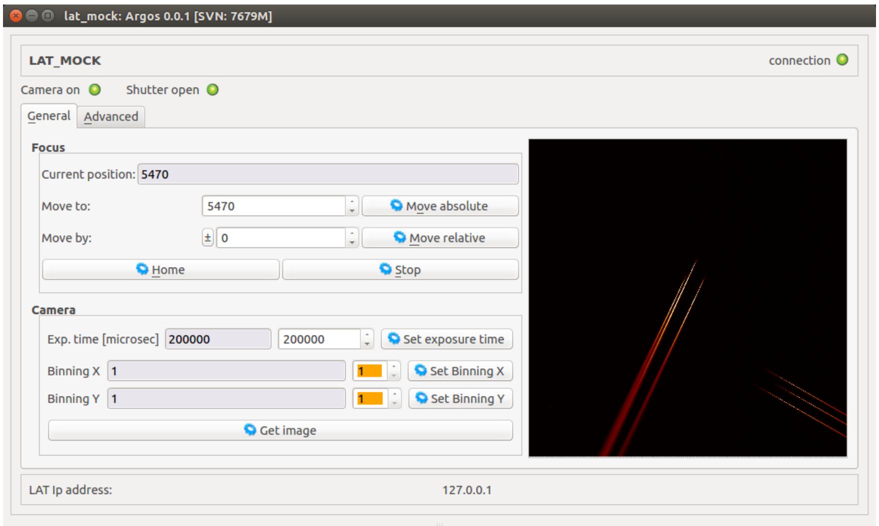

(a) General LAT GUI tab that allows changing the focus position, exposure time, and camera binning factors, in addition to capturing an image that is then displayed on the right. This image can be optionally saved as a .fits file.

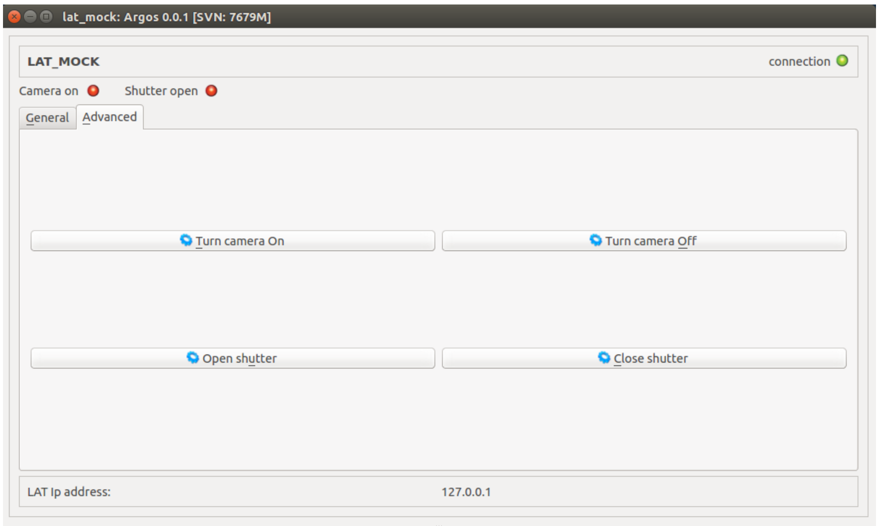

(b) Advanced LAT GUI tab that allows turning on and off the camera in addition to opening and closing the dust-shutter.

Figure 13.2: Screenshot of the ARGOS LAT GUI

Part IV

Status and Conclusion

14 Status and Conclusion

While implementing the LAT and SLA, certain complications arose that required adjustments and/or modifications to the original project plan. Some of these issues were immediately fixed while others have proven themselves beyond the scope of this masters project. This part will present a few of these issues and what has been done or needs to be in order to address them in the future. Chapter 15 tells the story of the failing DSC focus mechanism that crippled the LAT soon after installation on the LBT. The following chapter 16 explains the problems we had regarding the laser Target and its dependence on proper LBT optics collimation. In chapter 17 we will finally explore the astigmatism and coma of the LAT that we have referred to several times. Next in chapter 18 we will go over what progress has been made with height analysis of the lasers and how it could help the SLA. Finally, we will conclude the thesis in chapter 19.

15 Focus Friction Drive

After the LAT was installed onto the LBT, a technical issue presented itself where the focus motor would only function correctly when the LBT was at horizon. As the LBT increased elevation, the LATServer software would report the end limit-switch as triggered and the focus position would move indefinitely to step positions over 9000, which according to subsection 6.3.3 is an indication that something has gone wrong . Upon visual inspection with the housing cover removed and the LBT at zenith, it was discovered that the focus tube was slipping out of the LAT upon the slightest adjustment and slamming into the end limit. Further inspection revealed that dust contamination had caused a deep scratch in the friction plate on the DSC focuser, causing it to slip freely against the spring-loaded adjustment rod. The LAT was fully removed from the housing and disassembled so the friction plate could be taken out and re-smoothed. As of writing, plans are underway in Garching to adapt the DSC focuser to a rack and pinion system to prevent a similar situation in the future, but in the meantime keeping the cover on and dust-shutter closed should prevent re-contaminating the friction plate to the point of repeating the damage and resultant focus malfunction.

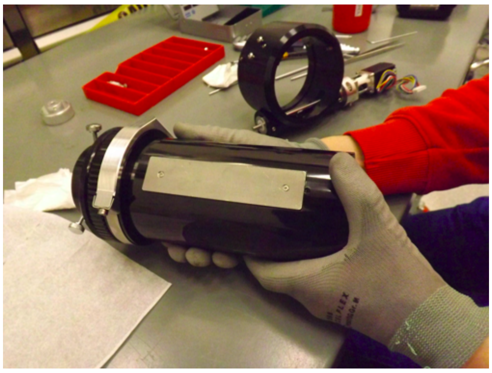

(a) Re-smoothed friction plate on focus tube

(b) Spring-loaded adjustment rod on the bottom inside the DSC focus sleeve.

Figure 15.1: Dissecting the troublesome DSC focuser. Note that the friction plate on the left had a deep scratch previously that made it slip against the adjustment rod on the right.

16 Optics Collimation

Once the SLA was integrated with ARGOS, the SLA could be initiated upon request and a successful alignment would be indicated by the presence of light in our patrol cameras (see figure 2.3). Soon after implementing the SLA, it was found that from one night to the next, our target position (see table 12.3) would consistently need updating as the lasers were being positioned to the wrong locations. We were often required to manually align the lasers into the patrol cameras, record the new target position, achieve automated success with the SLA over a few hours, then repeat the process all over again with a false target. We decided to plot the new targets over two nights, which produced the plot in figure 16.1.

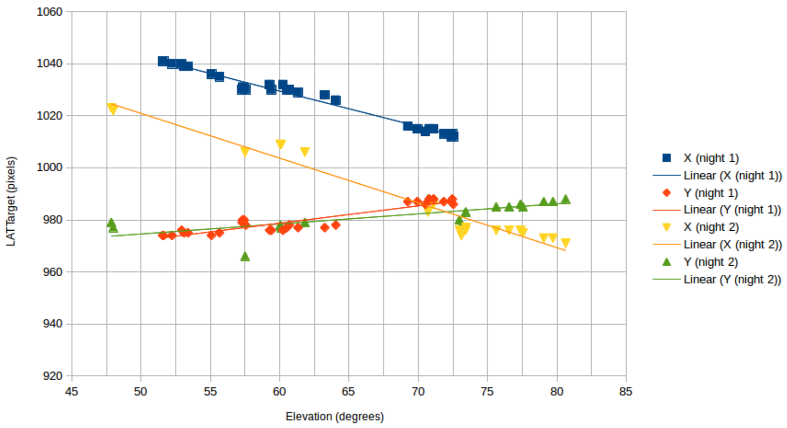

Figure 16.1: Laser endpoint targets recorded over two separate nights. Notice the obvious offset between the x-coordinates over the two nights (blue squares vs yellow triangles).

The plot suggested that there was an offset being created between the LAT and the LBT optics, especially in along the azimuthal direction. It was discovered that upon changing celestial targets throughout the night, the Telescope Operator would not always reset the optics through a collimation procedure and instead just jump straight between targets. This caused a series of offsets to accumulate between the LBT mount (to which the LAT is aligned) and the LBT optics (to which the WFS is aligned). As we see in the plot, this offset can grow as high as 30 pixels or above 50", which exceeds our 30" error budget for the laser endpoint target. It was necessary to add the collimation procedure to future instances of target changes for ARGOS if the SLA is to function correctly. With the resetting of the LBT optics to a consistent zero-position, the accumulated misalignment offset has appeared to vanish.

17 Optical Aberrations

17.1 Astigmatism

Recall that during our testing phase with the ProtoLAT, we tried to calculate the focus position of the LAT that would place the camera at the true focal length of the telescope (see subsection 7.1.3). The original intention was to fit a curve to these points with positive concavity such as a parabola or hyperbola from which the optimized absolute minimum would give the position for a focused LAT. The figure failed to produce an absolute minimum, however, and instead gave two local minima with a local maximum in between.

From here we determined that the cause of this must stem from astigmatism in the LAT optics, or a deviation from spherical curvature in its lens that causes incoming light rays with perpendicular planes of propagation to focus at different lengths (Born et al. [2000]). This would mean that the star light from Arcturus propagating parallel to the angle of astigmatism would focus at a different length than that propagating perpendicular, which is exactly what we witness in the plot of figure 7.8 with the two local minima.

This astigmatism prevented us from finding an absolute focus position that focuses the LAT camera to infinity, but the SLA was not noticeably impacted by this and a fix will not be sought after.

17.2 Coma

Upon taking the first images with the ProtoLat, we found that smaller stars lacked a clean round shape and would instead appear a bit more triangular (see figure 17.1). This is a known aberration of coma where the telescope optics have a misalignment between the lens, causing off-axis targets to become asymmetric with a characteristic flared edge (Born et al. [2000]). Unlike the astigmatism, this effect did have a slight impact on implementation of the SLA. As most of the light from the laser beams is off-axis to the LAT, we can see the coma effect cause asymmetry as in figure 17.2. This asymmetry leads to Gaussian fits in the Gaussian-Subtraction method of the SLA not being as close as desired. In addition, the Skeleton method could not correctly find laser peaks since the edges of the lasers were unequal distances from them. As of writing, plans are underway to take down the LAT during the next commissioning run and replacing it with an identical telescope with optics that have been aligned by the engineers at the MPE.

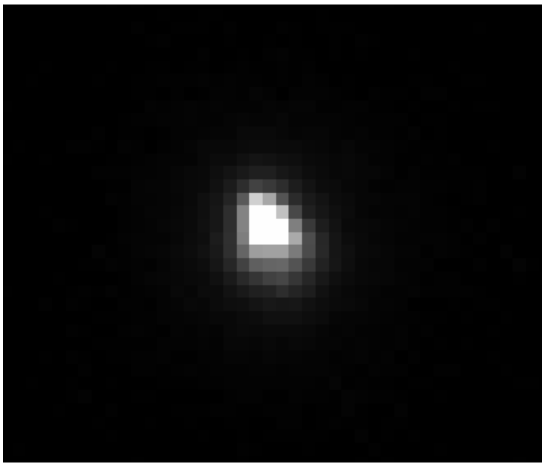

Figure 17.1: LAT image closeup of a random star. Note the triangular shape as opposed to the expected roundedness of a star. This is typical of optical coma.

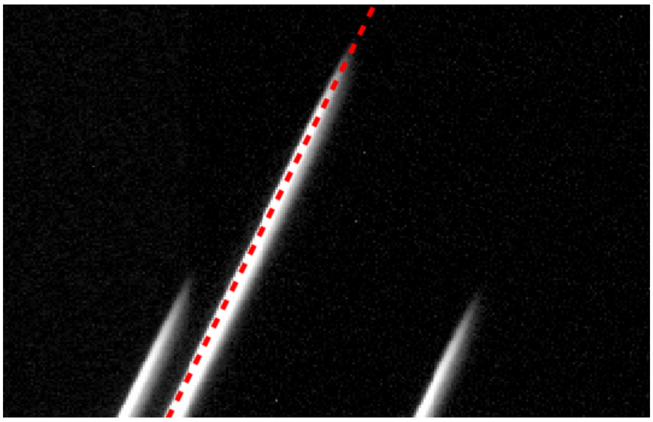

Figure 17.2: A closeup of a LAT image with lasers present and a dashed line plotted along the maxima peaks of the middle laser. Note the asymmetry caused by the coma where more laser light appears smeared to the right of the line. This had some noticeable effect while developing the SLA.

18 Height Analysis

One complication that arises from the end point target alignment scheme is the presence of clouds in the path of the laser beams, causing extra Rayleigh scattering at lower atmospheres and ultimately a greater attenuation of each beam along its respective line of travel. This causes the endpoints of the beams to be located at a shorter distance along the beam than on a clear night, effectively causing error in our endpoint target (see figures 18.1 and 18.2).

The proposition to fix this shortcoming of the endpoint alignment scheme was to fit a Rayleigh scattering model to the lasers' integrated flux profiles up to where the cloud anomaly starts. The remaining profile of the laser could then be extrapolated to where the laser end point would have been located had the clouds not been present (see figure 18.2). Of course such a model would be dependent on a physical height of the imaged laser as opposed to the projected laser onto the CCD we currently use. We would first need to transform pixels to kilometers with some geometric analysis, from which we use the laser geometry itself and equations derived from it.

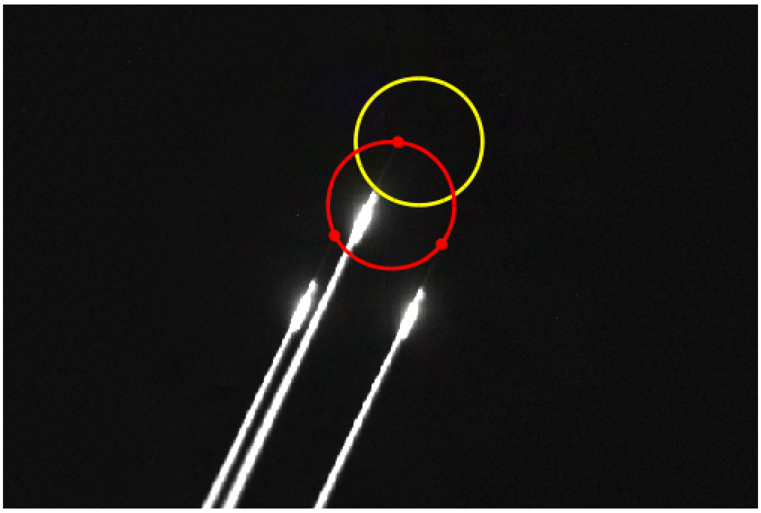

Figure 18.1: Image of lasers that are correctly aligned with the WFS, but the SLA is locating them at the red circle and incorrectly asking that they move to the Target at the yellow circle. This is because of the lower calculated endpoints caused by clouds scattering photons that would normally extend the beams all the way to the yellow circle.

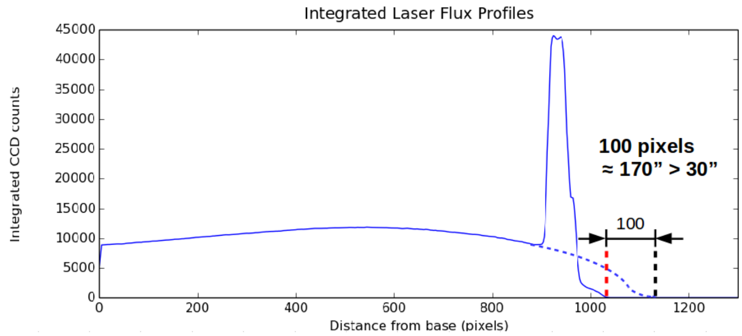

Figure 18.2: Integrated flux profile of one of the lasers above with clouds in the path of propagation. The dashed blue profile shows how the profile would normally continue to the dashed black line, but is instead cut short by the excess scattering at lower altitudes. Note the shortened laser beam puts our Target 170" away from a successful alignment, which is much greater than our error budget of 30" allows.

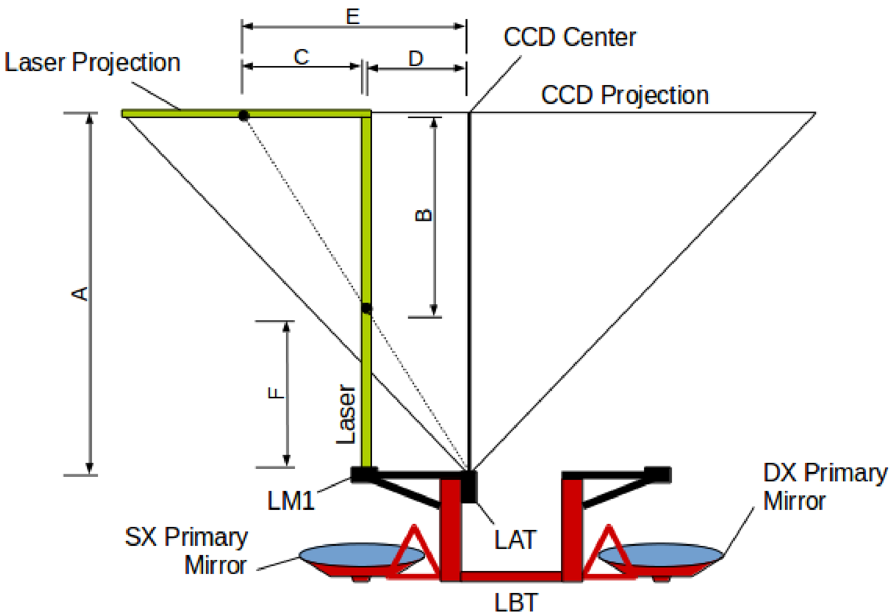

Figure 18.3: Drafted diagram on the laser geometry as projected onto the LAT CCD. Here we visualize the LAT CCD as being projected onto the sky at the altitude A where the laser endpoints are located. From here we can calculate F, the height along the laser, as a function of A.

By looking at the geometry in figure 18.3, we see that distance F is our desired dimension for length along the laser beam. By use of similar triangles, we calculate that

$$\frac{B}{C} = \frac{A}{E} \tag{18.1}$$

or

$$B = \frac{A * C}{E} \tag{18.2}$$

And since F is calculated as

$$F = A - B \tag{18.3}$$

we end up with

$$F = A\Big(1 - \frac{C}{E}\Big) \tag{18.4}$$

Now keep in mind that C and E are physical distances, but we want to project them onto the CCD to get the distances in pixels as C_{pix} and E_{pix}. To do this, we would use the pixel scale of the LAT (1.7" or 8.24 μrad) and, because C and E will form such small angles, we can estimate that multiplying these angles by A will convert to their physical distances. So we get

$$C = 8.24 \times 10^{-6} A C_{pix} \tag{18.5}$$

$$E = 8.24 \times 10^{-6} A E_{pix} \tag{18.6}$$

which we see leads to the conversion constants simply being canceled out in equation 18.4, leaving us with

$$F = A\Big(1 - \frac{C_{pix}}{E_{pix}}\Big) \tag{18.7}$$

We can apply this transform to previous integrated flux profiles by calculating C_{pix} and E_{pix} for each point along the laser and plotting the profile with F, which we can define as a fraction of A. Upon applying this to a previous integrated flux profile, namely to the top one in figure 11.1, we can get a more physical picture of the returned laser light on our LAT CCD in figure 18.4.

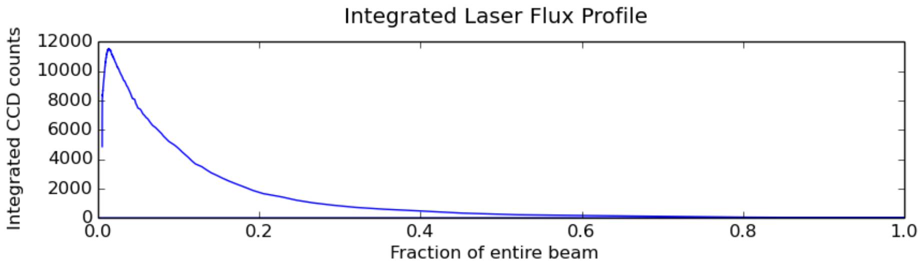

Figure 18.4: Flux profile of the top laser from figure 11.1 with the transform in equation 18.7 applied. Note that without knowing what A (the height of the laser endpoints) is in the transform , we cannot have a physical altitude on the x-axis. Instead, we define F as a fraction of A.

We see from the returned laser beam flux an initial increase to a maximum followed by what resembles an inverse square relation to position along the beam. This is promising, because it means that our integrated flux profiles can be modeled by the Light Detection And Ranging (LIDAR) equation, a scattering model used in optical surveying technologies. This model integrates the inverse square feature of light and the scattering coefficients and density of the atmosphere, in addition to an "overlap" efficiency coefficient where laser light entering a CCD from the edges will have a fraction of its photons not reach the CCD, effectively causing the initial positive slope in the figure 18.4 that crests to a maximum before falling off. The LIDAR equation derived by Rabien et al. [2008] into a very simplified form is

$$N_{ph} = \frac{ED^2 \rho(z) \frac{d\sigma}{d\Omega} \Delta z}{\gamma z^2} \tag{18.8}$$

where N_{ph} are the number of photons detected by the pixel, z is the altitude of the section of the laser beam imaged by the pixel, Δz is how much length of the laser beam is imaged by the pixel, E is the energy of a laser beam pulse, $\rho(z)$ is the density of the atmosphere at the current z, D is the diameter of the LAT aperture, $\frac{d\sigma}{d\Omega}$ is the atmosphere particle scattering cross-section, and γ is the efficiency coefficient. The density can be found from the 1976 United States Standard Atmosphere measurements (USSA [2014]). The scattering cross-section can be simplified to Rayleigh scattering, as that is the main mechanism at work with the ARGOS lasers. That just leaves the unknown efficiency factor γ, which can be estimated with LAT laser images where the height of the clouds is bounded by their presence on the WFS, which we know is gated at 12km.

Taking this exercise further, however, is beyond the scope of this masters thesis and will be put to future users hoping to expand the capabilities of the SLA to cloudy conditions.

19 Conclusion

Despite the minor issues still facing the LAT and its complimentary SLA algorithm, the project overall was a success. During the previous two commissioning runs, the ARGOS team has saved an estimated 3 hours in accumulated alignment time over 10 days of laser use. With the planned upgrades to the hardware, fine-tuning of the SLA parameters, and eventual addition of the height analysis, the LAT promises to be an essential component to ARGOS and the LBT as a whole.

Upon joining the ARGOS team, I initially had the goal to not only successfully implement the instrument I was tasked to complete, but to gain familiarity with software development that would compliment my knowledge of physics upon entering the tech industry. This project not only required me to develop skills in object oriented programming languages, hardware-software control interfaces, software design and development, and the new machine-learning field of computer vision, but it also put me into such unique work conditions that few people could hope to experience. Needing to patch one's own software under low oxygen conditions, as well as juggling an astronomer's demanding sleep and travel schedule — all while sitting at the controls of one of the world's largest telescopes — was as rewarding for a graduate student as it was taxing.

What I find most fulfilling about my project is that I walked away with not only a thesis to show the planning and execution necessary to prove my skills in the crucial instrumentation branch of astronomy, but also a new ignited passion for gazing at the stars. There is something rather romantic about spending summer nights on the roof of one's astronomical institute with naught but a telescope and the celestial heavens above. This was especially meaningful as it was necessary for the project, placing me among those who have contributed to humanity's pursuit of knowledge.

I find the feeling I have after finishing this project can be summed up by one of my favorite quotes:

"The surface of the Earth is the shore of the cosmic ocean. On this shore, we've learned most of what we know. Recently, we've waded a little way out, maybe ankle-deep, and the water seems inviting." -Carl Sagan

Part V

Appendix

A Glossary

altitude or elevation. The angle formed between the observer's line of sight and the horizon. The measurement starts at 0 degrees at horizon and ends at 90 degrees at zenith (straight above the observer). Note that the altitude of LBT is limited between 45 degrees and zenith when operating the ARGOS lasers..

AO Adaptive optics. An optical technology used with astronomical instruments to diminish the effect of wavefront distortions caused by atmospheric turbulence. .

ARGOS Advanced Rayleigh guided Ground layer adaptive Optics System. An AO system in commission at the LBT that used six Rayleigh laser guide stars (three for each LBT mirror). .

azimuth The angle along the circle formed along the horizon around the observer in the horizontal coordinate system. The measurement starts at 0 degrees pointing north and increases to 360 degrees in the clockwise direction. .

binning Feature of a camera where adjacent pixels are summed according to the binning factor. This decreases the readout time of the CCD for a trade-off in spatial resolution..

Dec Declination. The dimension aligned with earth's latitude lines in the equatorial coordinate system to locate celestial objects. Ranges from -90 degrees at the southern celestial pole to +90 degrees at the northern celestial pole with the celestial equator sitting at 0 degrees..

DSC Dual Speed Crayford. A type of focusing mechanism commonly reserved for higher-level amateur telescope systems. The DSC works similar to a a rack and pinion adjustment system, but without teeth. A spring-loaded rod controlled by the focus knobs smoothly moves a flat plate embedded in the focus tube by friction, allowing the focus to be adjusted without wobble or backlash .

FOV Field of View. The two angle dimensions of the solid angle that can be imaged by an optical instrument.

FWHM Full width at half maximum. A quantity that can be attributed to a distribution defined as the difference between the independent variables where the dependent variable is equal to half of its maximum value..

ICE Internet Communications Engine. An open source software framework maintained by ZeroC that allows creation of server/client interfaces written in differing programming languages (++, C#, Java, JavaScript, Objective-C, PHP, Python, or Ruby) and implemented on different operating systems (Windows, OS X, and Android)..

IP Internet Protocol. The network communications rules system standard we use when addressing locations in the network..

LAT Laser Alignment Telescope. The instrument that was built for this masters project. Used to align ARGOS lasers in addition to whatever other use the LBT staff and observers have for it..

LGS Laser Guide Star. A slice taken of each laser at 12km along the beams that are imaged on the wavefront sensors. These slices produce artificial stars so ARGOS can map their wavefronts in order to quantify and correct for atmospheric turbulence with the deformable mirrors of LBT.

LM1 Primary Launch Mirror. Mounted on the back of the LBT secondary mirrors, these launch mirrors (one for each LBT side) are our main adjustment mechanism for altering the direction of the ARGOS laser triplets.

MAT Mount Alignment Telescope. The predecessor to the LAT used by the LBT to aid in problems with telescope pointing or to monitor clouds crossing the LBT target field. Contains two telescopes, one with a narrow-field (MAT-NF) and the other with a wide-field (MAT-WF). .

MPE Max Planck Institute for Extraterrestrial Physics. .

MPIA Max Planck Institute for Astronomy. .

RA Right ascension. The dimension aligned with earth's longitude lines in the equatorial coordinate system to locate celestial objects. It forms a complete circle with 0 starting where the Sun crosses the celestial equator at the March equinox. Can be counted up to 24 hours or 360 degrees..

SLA Smart Laser Alignment. The alignment algorithm written for this masters thesis. The algorithm scans row by row an image of the ARGOS lasers taken by the LAT, locates the lasers, calculates their endpoints, and transmits to the LM1 controller how much it should move to align the 12km points of the lasers to the ARGOS wavefront sensors..

SX/DX Nicknames for the left and right sides of the LBT. Stems from the Italian words sinistra (left) and destra (right)..

WFS Wavefront sensor. The devices (one for each LBT side) that image the LGSs after splitting the artificial starlight through lenslet arrays. This allows the wavefronts to be mapped and the information is sent to the deformable mirrors of LBT to compensate..

B Test Client User Guide

Command	Argument 1	Argument 2	Description
CamPowerOn			Turns on camera
CamPowerOff			Turns off camera
CamPowerStat			Outputs to CL whether camera is on or off
ShutterOpen			Opens dust shutter
ShutterClose			Closes dust shutter
ShutterStat			Outputs to CL whether dust shutter is open or closed
FocHome			Resets focus position to home
FocMoveAbs	$0 \leq$ [Integer] ≤ 9000		Moves focus to given step position
FocMoveRel	$-9000 \leq$ [Integer] ≤ 9000		Moves focus given number of steps from current position. Negative is towards home.
GetImage			Takes image with camera, saving as .fits file in directory indicated by included client.config file
GetCamParam	ExpTime		Outputs camera exposure time in microseconds to CL
SetCamParam	ExpTime	$75 \leq$ [Integer] ≤ 53700000	Sets camera exposure time in microseconds
GetCamParam	BinningX		Outputs to CL camera horizontal binning factor
SetCamParam	BinningX	$1 \leq$ [Integer] ≤ 8	Sets camera horizontal binning factor
GetCamParam	BinningY		Outputs camera vertical binning factor to CL
SetCamParam	BinningY	$1 \leq$ [Integer] ≤ 2048	Sets camera vertical binning factor

Table B.1: Command arguments used with the LATClient test client program

C Motor Serial Commands

Reference run

Command	Response	Description
#<motor>p4	<motor>p4	Set positioning mode external reference run
#<motor>d0	<motor>d0	Sets the direction of rotation: 0: Left
#<motor>A	<motor>A After completing movement: status of the firmware as a bit mask	Starting motor
#<motor>:is_referenced	<motor>:is_referenced+1	If the motor has already been referenced, '1' is returned, otherwise '0'.
#<motor>C	<motor>C[max +/- 100000000]	Returns the current position

Example:

#1p4	1p4
#1d0	1d0
#1A	1A
#1:is_referenced	1:is_referenced
#1C	1C+0

Relative positioning

Command	Response	Description
#<motor>p1	<motor>p1	Set positioning mode relative positioning
#<motor>d[0/1]	<motor>d[0/1]	Sets the direction of rotation: 0: Left 1:right
#<motor>s[0 to +100,000,000]	<motor>s[0 to +100,000,000]	This command specifies the travel distance in (micro-)steps. Only positive values are allowed for the relative positioning. The direction is set with command 'd'.
#<motor>A	<motor>A After completing movement: status of the firmware as a bit mask	Starting motor
1	<motor>C[max +/- 100000000]	Returns the current position

Figure C.1: First set of motor commands for stepper motor controller. A command begins with the start character '#' and ends with a carriage return '\r'. These can be sent using telnet or as strings over network sockets. Commands are continued on the next page. Table courtesy of Ziegleder [2015].

Absolute positioning

Command	Response	Description
#<motor>p2	<motor>p2	the specified position is moved to as an absolute position
#<motor>s[0 to +100,000,000]	<motor>s[0 to +100,000,000]	This command specifies the travel distance in (micro-)steps. Only positive values are allowed for the relative positioning. The direc tion is set with command 'd'.
#<motor>A	<motor>A After completing movement: status of the firmware as a bit mask	Starting motor
#<motor>C	<motor>C[max +/- 100000000]	Returns the current position

How to recover after occurrence of a position error

#<motor>$ reports a Position error by rising bit 3.

Command	Response	Description
#<motor>C	<motor>C[max +/- 100000000]	Returns the current position
#<motor>D[max +/- 100000000]	<motor>D	Resetting the position error, set counter to last position. See 1.5.17

It is strongly recommended to start a reference run afterwards

Setting the outputs

Command	Response	Description
#<motor>Y	Confirms the command through an echo.	The status of the inputs and outputs are combined in a 32bit (integer) bitmask. Bit 16: Output 1, dust shutter pneumatic valve Bit 17: Output 2, camera power See 1.5.30

Reading input and output status

Command	Response	Description
#<motor>ZY	#<motor>ZY[0 to 4294967295]	The status of the inputs and outputs are combined in a 32bit (integer) bitmask. Bit0: Input 1, endstop at camera side Bit1: Input 2, endstop at motor side Bit 2..15: ignore Bit 16: Output 1, dust shutter pneumatic valve Bit 17: Output 2, camera power Bit 18..32: ignore

How to safely set an output

Command	Response	Description
#<motor>ZY	#<motor>ZY[0 to 4294967295]	Read the input and output status
		Change bit 16 or 17 to the desired value, leave all other bits unchanged
#<motor>Y[modified bitmask]	Confirms the command through an echo.	Write the modified bitmask to the controller.

Else

Command	Response	Description
#<motor>$	status of the firmware as a bit mask The bit mask has 8 bits.	Bit 0: 1: Controller ready Bit 1: 1: Zero position reached Bit 2: 1: Position error Bit 3: 1: Input 1 is set while the controller is ready again. This occurs when the controller is started via input 1 and the controller is ready before the input has been reset. Bits 4 and 6 are always set to 0, bits 5 and 7 are always set to 1. See 1.5.22.
#<motor>v		Reading out the firmware version (communication check). See 1.5.23.

Figure C.2: First set of motor commands for stepper motor controller continued from figure C.1. Table courtesy of Ziegleder [2015].

D Lists

D.1 List of Figures

D.2 List of Tables

E Bibliography

ARGOS. Gallery, May 2014. URL http://www.mpe.mpg.de/1192377/gallery.

M. Born, E. Wolf, A.B. Bhatia, D. Gabor, A.R. Stokes, A.M. Taylor, P.A. Wayman, and W.L. Wilcock. *Principles of Optics: Electromagnetic Theory of Propagation, Interference and Diffraction of Light*. Cambridge University Press, 2000. ISBN 9780521784498.

Jay L. Devore and N.R. Farnum. *Applied statistics for engineers and scientists*. Statistics Series. Duxbury Press, 1999. ISBN 9780534356019.

S. Esposito, A. Riccardi, E. Pinna, A. Puglisi, F. Quirós-Pacheco, C. Arcidiacono, M. Xompero, R. Briguglio, G. Agapito, L. Busoni, L. Fini, J. Argomedo, A. Gherardi, G. Brusa, D. Miller, J. C. Guerra, P. Stefanini, and P. Salinari. Large Binocular Telescope Adaptive Optics System: new achievements and perspectives in adaptive optics. In *Astronomical Adaptive Optics Systems and Applications IV*, volume 8149 of *Proc. SPIE*, page 814902, October 2011. doi: 10.1117/12.898641.

John Hill. Using mat - the mount alignment telescopes, 2015. URL http://wiki.lbto.org/bin/view/Operators/UsingMAT. [Online; accessed 28-April-2016].

Steve B Howell, Richard Ellis, John Huchra, Steven Kahn, George Rieke, and Peter B Stetson. *Handbook of CCD Astronomy; 2nd ed.* Cambridge Univ. Press, Cambridge, 2006.

J. A. Högbom. Aperture synthesis with a non-regular distribution of interferometer baselines. *Astronomy and Astrophysics Supplement*, 15:417, 1974.

P. Léna, D. Rouan, F. Lebrun, F. Mignard, D. Pelat, L. Mugnier, and S.N. Lyle. *Observational Astrophysics*. Astronomy and Astrophysics Library. Springer Berlin Heidelberg, 2012. ISBN 9783642218156.

S. Rabien, N. Ageorges, R. Angel, G. Brusa, J. Brynnel, L. Busoni, R. Davies, M. Deysenroth, S. Esposito, W. Gässler, R. Genzel, R. Green, M. Haug, M. Lloyd Hart, G. Hölzl, E. Masciadri, R. Pogge, A. Quirrenbach, M. Rademacher, H. W. Rix, P. Salinari, C. Schwab, T. Stalcup, Jr., J. Storm, L. Strüder, M. Thiel, G. Weigelt, and J. Ziegleder. The laser guide star program for the LBT. In *Adaptive Optics Systems*, volume 7015 of *Proc. SPIE*, page 701515, July 2008. doi: 10.1117/12.788173.

S. Rabien, N. Ageorges, L. Barl, U. Beckmann, T. Blümchen, M. Bonaglia, J. L. Borelli, J. Brynnel, L. Busoni, L. Carbonaro, R. Davies, M. Deysenroth, O. Durney, M. Elberich, S. Esposito, V. Gasho, W. Gässler, H. Gemperlein, R. Genzel, R. Green, M. Haug, M. L. Hart, P. Hubbard, S. Kanneganti, E. Masciadri,

J. Noenickx, G. Orban de Xivry, D. Peter, A. Quirrenbach, M. Rademacher, H. W. Rix, P. Salinari, C. Schwab, J. Storm, L. Strüder, M. Thiel, G. Weigelt, and J. Ziegleder. Argos: the laser guide star system for the lbt. In *Adaptive Optics Systems II*, volume 7736, pages 77360E–77360E–12, 2010. doi: 10.1117/12.857210. URL http://dx.doi.org/10.1117/12.857210.

USSA. Properties of the u.s. standard atmosphere 1976, Feb 2014. URL http://www.pdas.com/atmos.html.

J. Ziegleder. Argos - easy ao introduction, Jul 2009. URL http://www2011.mpe.mpg.de/ir/projects/lbtlaser/intro_easy.php.

J. Ziegleder. *Laser Alignment Telescope (LAT) controller manual.* ARGOS, a edition, 8 2015.

Erklärung:

Ich versichere, dass ich diese Arbeit selbstständig verfasst habe und keine anderen als die angegebenen Quellen und Hilfsmittel benutzt habe.

Heidelberg, den (Datum) ....